ROM SAF Report 17
Ref: SAF/ROM/METO/REP/RSR/017
Web: www.romsaf.org
Date: 21 Dec 2015

The EUMETSAT Network of Satellite Application Facilities

ROM SAF
Radio Occultation Meteorology

ROM SAF Report 17

Simulation of L1 and L2 bending angles with a model ionosphere

I D Culverwell[1] and S B Healy[2]

[1]Met Office, Exeter, UK
[2]ECMWF, Reading, UK

Document Author Table

	Name	Function	Date	Comments
Prepared by:	I D Culverwell	ROM SAF Project Team	21 Dec 2015	
Reviewed by:	M Forsythe	Met Office	1 Nov 2015	
Reviewed by:	R Saunders	Met Office	14 Dec 2015	
Approved by:	K B Lauritsen	ROM SAF Project Manager	21 Dec 2015	

Document Change Record

Issue/Revision	Date	By	Description
0.1	6 Mar 2014	IDC	First draft
0.2	31 Jan 2015	IDC	Remove all but simplest large l' expansion
0.3	31 Jul 2015	IDC	Add further toy model test; incorporate MF's corrections
0.4	31 Aug 2015	IDC	Include App C on reformulation of Z(l)
1.0	21 Dec 2015	IDC	Final release

ROM SAF

The Radio Occultation Meteorology Satellite Application Facility (ROM SAF) is a decentralised processing centre under EUMETSAT which is responsible for operational processing of GRAS radio occultation data from the Metop satellites and RO data from other missions. The ROM SAF delivers bending angle, refractivity, temperature, pressure, and humidity profiles in near-real time and offline for NWP and climate users. The offline profiles are further processed into climate products consisting of gridded monthly zonal means of bending angle, refractivity, temperature, humidity, and geopotential heights together with error descriptions.

The ROM SAF also maintains the Radio Occultation Processing Package (ROPP) which contains software modules that will aid users wishing to process, quality-control and assimilate radio occultation data from any radio occultation mission into NWP and other models.

The ROM SAF Leading Entity is the Danish Meteorological Institute (DMI), with Cooperating Entities: i) European Centre for Medium-Range Weather Forecasts (ECMWF) in Reading, United Kingdom, ii) Institut D'Estudis Espacials de Catalunya (IEEC) in Barcelona, Spain, and iii) Met Office in Exeter, United Kingdom. To get access to our products or to read more about the project please go to: http://www.romsaf.org

Intellectual Property Rights

Abstract

This report describes the modelling of the L1 and L2 bending angles by means of a simple idealised ionosphere consisting of a single Chapman layer. There are three main reasons for doing this:

- The desire for an improved interpolation/extrapolation of the L1 – L2 bending angle difference where either signal (but especially L2) drops out;
- The wish to make retrievals using observational data that are closer to what is observed, rather than the ionospherically corrected neutral bending angles that are usually used;
- It allows the sensitivity of the observed bending angles with respect to the unknown ionospheric parameters to be assessed.

Sensitivities to horizontal gradients and to the shape and size of the model ionosphere are briefly examined before calculating the bending angles induced by a single Chapman layer. The feasibility of making retrievals directly with L1 and L2, and with L1 alone, are studied in a simple 'toy' system, and the results are compared against retrievals made in the same system with the usual ionospherically corrected bending angles. All GRAS occultations within a five day period have their L1 – L2 bending angle differences modelled by this theory, and the derived ionospheric parameters are examined. Areas for further study are suggested.

Contents

1 Introduction

Above about 60 km, the ionosphere generally makes the biggest contribution to the bending of radio occultation (RO) signals. This bending is usually removed during pre-processing of the signals from the two (L1 and L2) RO channels, by exploiting the dispersive nature of the ionosphere to radio waves. This isolates the bending produced by the neutral atmosphere, which is of greater interest in most cases.

Sometimes, however, the L2 signal drops out, especially at lower altitudes. Some sort of extrapolation of the observed signal is therefore required before it can be combined with the L1 signal in order to remove the ionospheric contribution to the bending. Direct modelling of the ionospheric bending of the two signals might offer a better way of doing this extrapolation than the current procedure — linear extrapolation of L1 – L2 — because it would be based on all the available profile information, not just that in the locality of the missing data. It might also offer the possibility of using either signal, or both, directly, without the need for any ionospheric correction. L1 and L2 have smaller fractional errors above about 60 km than the very small neutral bending angle at these heights. This may or may not lead to better retrievals. Finally, direct modelling of the ionosphere might offer the possibility of retrieving some information about the ionosphere from RO profiles.

For all these reasons, it is worth examining the bending angles produced by a model ionosphere. This report describes some first steps along that path. Sec 2 describes the background theory of ionospheric bending, and pays particular attention to the effects of spherical asymmetry. Sec 3 examines the sensitivity of the bending angles to the size and shape of a spherically symmetric ionosphere, before Sec 4 reports details of the bending induced by one particular model ionosphere — a Chapman layer — which forms the basis of the later work in the report. The detailed calculations appear in Apps A and B. Secs 5 and 6 present the results of some preliminary studies using these ideas on idealised and real RO data respectively. Sec 7 summarises the work and suggests future areas of study.

2 Background theory

2.1 Spherically symmetric ionosphere

The usual formula for the bending angle α at impact parameter a in a spherically symmetric atmosphere of refractive index n is given by (eg Rodgers, 2000 [13]):

$$\alpha(a) = -2a \int_a^\infty \frac{\mathrm{d}\log n/\mathrm{d}x}{\sqrt{x^2-a^2}}\mathrm{d}x \tag{2.1}$$

where $x = nr$, and $\log n \approx n-1$ for $|n-1| \ll 1$.

In the ionosphere, radio waves excite plasma oscillations, which affect the phase and group velocities of the wave. The high frequency refractive index in such a medium, in the absence of electric or magnetic fields, is given by (eg Sec 32–7, Feynman, 1964 [7]):

$$n^2 = c^2k^2/\omega^2 = 1 - \omega_p^2/\omega^2 < 1 \tag{2.2}$$

where ω_p^2, the square of the plasma frequency, equals $n_e e^2/m_e\varepsilon_0$, n_e being the electron number density and the other symbols having their usual meanings.

In a plasma, therefore, $c_{\text{phase}} = \omega/k > c$ and $c_{\text{group}} = \mathrm{d}\omega/\mathrm{d}k = c^2/c_{\text{phase}} < c$.

Typically in the ionosphere, $n_e \sim 10^{12}$ m^{-3} which implies $\omega_p \sim 5\times10^7$ s^{-1}, while at RO frequencies $\omega = 2\pi f \sim 10^{10}$ s^{-1}, which means that $\omega_p \ll \omega$ so that we can write

$$n - 1 \approx \omega_p^2/2\omega^2 = -k_4 n_e/f^2 \tag{2.3}$$

where $k_4 = e^2/8\pi^2 m_e\varepsilon_0 = 40.3$ m^3 s^{-2}.

Therefore, the ionospheric contribution to the bending angle at frequency f is given by

$$\alpha(a) = 2a\frac{k_4}{f^2}\int_a^\infty \frac{\mathrm{d}n_e/\mathrm{d}x}{\sqrt{x^2-a^2}}\,\mathrm{d}x. \tag{2.4}$$

Naively integrating by parts, we obtain

$$\alpha(a) = 2a\frac{k_4}{f^2}\left[\frac{n_e(x)}{\sqrt{x^2-a^2}}\right]_a^\infty + 2a\frac{k_4}{f^2}\int_a^\infty \frac{x\,n_e(x)}{(x^2-a^2)^{3/2}}\,\mathrm{d}x. \tag{2.5}$$

We cannot usually integrate Eqn (2.1) by parts because a non-zero $n(a)$ would cause a divergence in both parts. But for a vertically localised region of refractivity, sited well above tangent points of interest, the first term in Eqn (2.5) vanishes and we are left simply with

$$\alpha(a) = 2a\frac{k_4}{f^2}\int_a^\infty \frac{x\,n_e(x)}{(x^2-a^2)^{3/2}}\,\mathrm{d}x. \tag{2.6}$$

Note that this is always positive, whatever the shape of $n_e(x)$. This is not entirely obvious from the original $\mathrm{d}n_e/\mathrm{d}x$ expression, Eqn (2.4). (The 'geometrical factor' $(x^2-a^2)^{-1/2}$ is clearly crucial here: without it, Eqn (2.4) would integrate to zero for sufficiently rapidly decaying $n_e(x)$.)

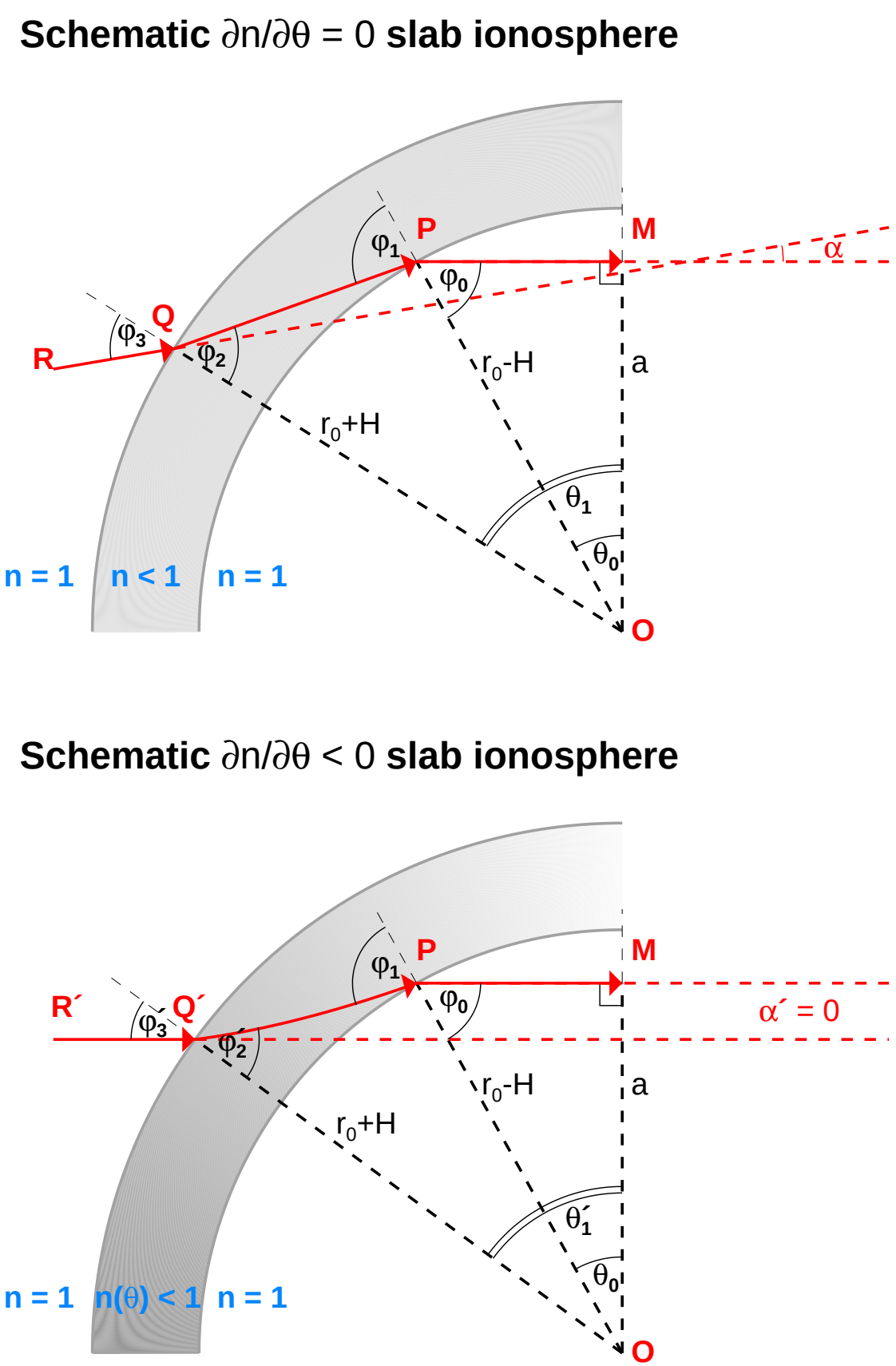

Figure 2.1: Schematic picture of ray bending. Top (a): spherically symmetric ionosphere. Bottom (b): ionosphere with constant horizontal refractive index gradient.

The physical reason for the positive sign of the bending follows from an examination of the bending induced by a 'slab' ionosphere — a uniform electron density between two spheres of radii $r_0 \pm H$, say. The geometry is shown in the top panel of Fig 2.1.

Note that the 'kicks' suffered by the ray as it enters and leaves the slab are of different sign, but that because $\phi_2 < \phi_1$, on account of the spherical geometry, $\phi_3 = \sin^{-1}(n\sin\phi_2) < \sin^{-1}(n\sin\phi_1) = \phi_0$. Hence the net kick is towards the Earth — that is to say, positive. Pictorially, the ionosphere is shaped locally like an upturned prism made of a material with $n < 1$, which means that this prism *diverges* the rays, and the bending is therefore towards the Earth. Since any spherically symmetric ionosphere can be thought of as an 'onion' of thin slabs like this, the bending must always be positive, as Eqn (2.6) shows mathematically. (This argument does not depend on PM being perpendicular to OM.)

We can easily calculate the bending caused by the slab ionosphere displayed in Fig 2.1a from first principles. Writing the ionospheric refractive index as $n = 1 - \delta$, where $\delta =$ const > 0 but $\ll 1$, and working to first order in δ, we have:

$$\text{Snell's law at } P\text{: } \sin\phi_0 = n\sin\phi_1 \implies \phi_1 = \phi_0 + \delta\tan\phi_0 \tag{2.7}$$

$$\text{Snell's law at } Q\text{: } \sin\phi_3 = n\sin\phi_2 \implies \phi_3 = \phi_2 - \delta\tan\phi_2 \tag{2.8}$$

$$\text{Bending: } \alpha = \phi_3 + \theta_1 - \pi/2 \quad \text{in general} \tag{2.9}$$

$$= (\phi_3 - \phi_2) + (\phi_1 - \phi_0) \quad \text{in this case, as } PQ \text{ is a straight line.} \tag{2.10}$$

These equations imply

$$\alpha = \delta\tan\phi_0 - \delta\tan\phi_2 \tag{2.11}$$

$$\approx \delta\sec^2\phi_0\,(\theta_1 - \theta_0) \quad \text{to first order in } (\theta_1 - \theta_0). \tag{2.12}$$

Now, $\sin\phi_2/(r_0 - H) = \sin\phi_1/(r_0 + H)$ (by the sine rule) $= \sin\phi_0/(r_0 + H) + O(\delta)$[1] $= a/(r_0^2 - H^2) + O(\delta)$. Thus, from Eqn (2.11), to first order in δ,

$$\alpha = a\delta\left[\left((r_0 - H)^2 - a^2\right)^{-1/2} - \left((r_0 + H)^2 - a^2\right)^{-1/2}\right] \tag{2.13}$$

$$= 2a\,\delta\,r_0 H(r_0^2 - a^2)^{-3/2} \quad \text{to first order in } H/r_0. \tag{2.14}$$

For future reference, the bending angle Eqn (2.13) can be expressed in terms of the vertically integrated total electron content, TEC, which is defined as

$$\text{TEC} = \int n_e \mathrm{d}r. \tag{2.15}$$

In this case, TEC $= 2H\delta(f^2/k_4)$, and therefore the bending angle in Eqn (2.13) can be written:

$$\alpha(a) = a\frac{k_4}{f^2}\frac{\text{TEC}}{2H}\left[\left((r_0 - H)^2 - a^2\right)^{-1/2} - \left((r_0 + H)^2 - a^2\right)^{-1/2}\right]. \tag{2.16}$$

[1] Note that $H/r_0 \sim 100/6700 \sim 1.5\%$, whereas $\delta \sim 10^{-5}$, so the 'geometry' effects dominate the 'refractivity' effects in these calculations. In reality, RQPM in Fig 2.1a is *very* nearly straight.

2.2 Effect of horizontal gradients

We briefly examine the effects of a weak violation of spherical symmetry, because horizontal gradients of electron density are often cited as a possible explanation of the *negative* ionospheric bending angles sometimes observed with the operational GRAS instrument (von Engeln, 2011 [17]).

In the presence of horizontal gradients, the path of the ray through the ionosphere is no longer straight. This clearly affects the entry angle ϕ_3 at Q. Might the overall bending now be negative? If so, how large a horizontal refractivity gradient would be needed for this to happen? To get a first answer to these questions, we examine the impact on the ray path of a small, uniformly varying refractive index in the slab ionosphere, as sketched in Fig 2.1b.

Thus, we postulate

$$n(\theta) = 1 - \delta_P + G(\theta - \theta_0), \tag{2.17}$$

and work to first order in the perturbation G. We therefore assume that the change in $(n-1)$ over the path is much less than $(n-1)$, ie that $|G(\theta_1 - \theta_0)| \ll \delta$.

In plane polar coordinates (r, θ), the Euler-Lagrange equation which results from applying Fermat's principle that the travel time between P and Q be stationary, ie

$$\delta \int n \, \mathrm{d}s = 0, \tag{2.18}$$

implies

$$\frac{\mathrm{d}}{\mathrm{d}r}\left\{\frac{nr^2\theta'}{\sqrt{1+(r\theta')^2)}}\right\} = \sqrt{1+(r\theta')^2}\,\frac{\partial n}{\partial \theta}. \tag{2.19}$$

If $\partial n/\partial\theta = G$ = constant, then, since $\mathrm{d}s/\mathrm{d}r = \sqrt{1+(r\theta')^2}$ and $\sin\phi = r\theta'/\sqrt{1+(r\theta')^2}$ (where ϕ is the angle between the radial vector and the direction of the ray), we have

$$nr\sin\phi - Gs = \text{constant} = (1-\delta_P)(r_0 - H)\sin\phi_1' - Gs_P \tag{2.20}$$

The quantity $nr\sin\phi - Gs$ is therefore the analogue of the impact parameter — the "constant of the motion" — when $\partial n/\partial\theta = G$ = constant. On the right hand side, the constant has been evaluated just inside the ionosphere at P in Fig 2.1b, where the ray has the angle of incidence ϕ_1' which is now given, by analogy with Eqn (2.7), by

$$\phi_1' = \phi_0 + \delta_P \tan\phi_0. \tag{2.21}$$

δ_P $(= \delta(\theta_0))$ in Eqn (2.21) equals δ in Sec 2.1; hence $\phi_1' = \phi_1$.

If $G = \partial n/\partial\theta = 0$, Eqn (2.20) correctly integrates to give $r(\theta) = (r_0 - H)\sin\phi_1 \csc(\phi_1 - (\theta - \theta_0))$: the straight line through P at the angle $\theta_0 + \phi_1$ to OM in Fig 2.1a. Following the perturbative approach described above, we therefore write

$$r(\theta)/(r_0 - H) = \sin\phi_1 \csc(\phi_1 - (\theta - \theta_0)) + Gg(\theta) \tag{2.22}$$

in the general case, where g is $O(1)$ and $g(\theta_0) = 0$ since the ray still passes through P. We seek the $g(\theta)$ which satisfies, to first order in G, Eqn (2.19). $n(\theta)$ is given by Eqn (2.17) and $r(\theta)$ by Eqn (2.22), which equation also shows that

$$\sin\phi = (1 + (r^{-1}\mathrm{d}r/\mathrm{d}\theta)^2)^{-1/2} = \sin\tilde{\phi}\left\{1 - G\sin\tilde{\phi}\cos\tilde{\phi}\csc\phi_1\left[g'(\theta)\sin\tilde{\phi} - g(\theta)\cos\tilde{\phi}\right]\right\}, \tag{2.23}$$

where $\tilde{\phi} = \phi_1 + \theta_0 - \theta$ is the 'straight line' value of ϕ, along PQ in Fig 2.1a.

The ray path distance from P, $s-s_P$, can be assumed to be the unperturbed value, since it is already multiplied by G in Eqn (2.20):

$$s(\theta)-s(\theta_0)=(r_0-H)\sin\phi_1\left[\cot\tilde{\phi}-\cot\phi_1\right]. \tag{2.24}$$

Substituting all these in Eqn (2.22) we get, to leading order in all small quantities,

$$g(\theta)=-1/2\cos\phi_1\csc^3\phi_1(\theta-\theta_0)^2 \tag{2.25}$$

Therefore, if $G=\partial n/\partial\theta<0$, $r(\theta)$ in Eqn (2.22) is greater than it would be in the spherically symmetric, unperturbed case, which makes sense.

The ray exits the ionosphere at the point Q', at angle θ_1' to OM in Fig 2.1b. This is given to leading order by

$$\theta_1'=\theta_1+1/2G\tan\phi_2\cos\phi_1\csc^3\phi_1(\theta_1-\theta_0)^2. \tag{2.26}$$

The angle of the ray to the normal at Q' is given, to first order in G and $(\theta_1-\theta_0)$, by

$$\phi_2'=\phi_2+G\cot\phi_1(\sin\phi_2/\sin\phi_1)^3(\theta_1-\theta_0). \tag{2.27}$$

Note that the path deviates from PQ by a term quadratic in $(\theta-\theta_0)$ (Eqn (2.25)), which means that its *direction*, which is what affects ϕ_2, varies linearly with $(\theta-\theta_0)$ (Eqn (2.27)). This dependence dominates the remaining calculations.

The angle of the ray on entry to the ionosphere at Q' is given by

$$\phi_3'=\phi_3+G\left(\tan\phi_2+\cot\phi_1(\sin\phi_2/\sin\phi_1)^3\right)(\theta_1-\theta_0), \tag{2.28}$$

by analogy with Eqn (2.8).

Finally, then, the overall bending is given, to first order in G and $\Delta\theta=(\theta_1-\theta_0)$, by

$$\begin{aligned}\alpha' &= \phi_3'+\theta_1'-\pi/2 \quad \text{by analogy with Eqn (2.10)}\\ &= \alpha+(\phi_3'-\phi_3)+(\theta_1'-\theta_1) \quad \text{also from Eqn (2.10)}\\ &= \delta_P(\tan\phi_0-\tan\phi_2)+G(\tan\phi_2+\cot\phi_1(\sin\phi_2/\sin\phi_1)^3)\Delta\theta,\end{aligned} \tag{2.29}$$

from Eqns (2.11), (2.26) and (2.28).

Thus, a sufficiently large negative horizontal refractive index gradient G could, in this theory, cause negative bending angles. The minimum such gradient is found by setting $\alpha'=0$ in Eqn (2.29). This is the situation sketched in Fig 2.1b. The mean TEC over PQ' is proportional to δ at the mid-point of PQ, $\delta_{PQ/2}$ say, $=\delta((\theta_1+\theta_0)/2)=\delta_P-G\Delta\theta/2$, which means that (using $\phi_3\approx\phi_2$ and $\phi_1\approx\phi_0$)

$$\alpha'\le 0 \implies G/\delta_{PQ/2} \le \frac{-2(\tan\phi_0-\tan\phi_2)}{(\tan\phi_0+\tan\phi_2+2\cot\phi_0(\sin\phi_2/\sin\phi_0)^3)\Delta\theta} \tag{2.30}$$

$$\to -\tan\overline{\phi} \quad \text{as } H\to 0, \tag{2.31}$$

where $\overline{\phi}$ is the angle between OM and the centre of $PQ^{(\prime)}$, ie $\tan\overline{\phi}=a/\sqrt{r_0^2-a^2}$.

The full expression on the right hand side of Eqn (2.30) is plotted in Fig 2.2 for a practical range of r_0, a and H. There is not a strong variation, and the expression is fairly well approximated by the limit in Eqn (2.31). This limit sheds an interesting physical light on the problem. For, if we were to ignore the curvature of the ray along PQ', and further assume that $Q\approx Q'$ and $\phi_2'\approx\phi_2$, then by analogy with Eqn (2.11) we would find the bending angle to be

$$\alpha'=\delta_P\tan\phi_0-\delta_Q\tan\phi_2=(\delta_{PQ/2}+G\Delta\theta/2)\tan\phi_0-(\delta_{PQ/2}-G\Delta\theta/2)\tan\phi_2 \tag{2.32}$$

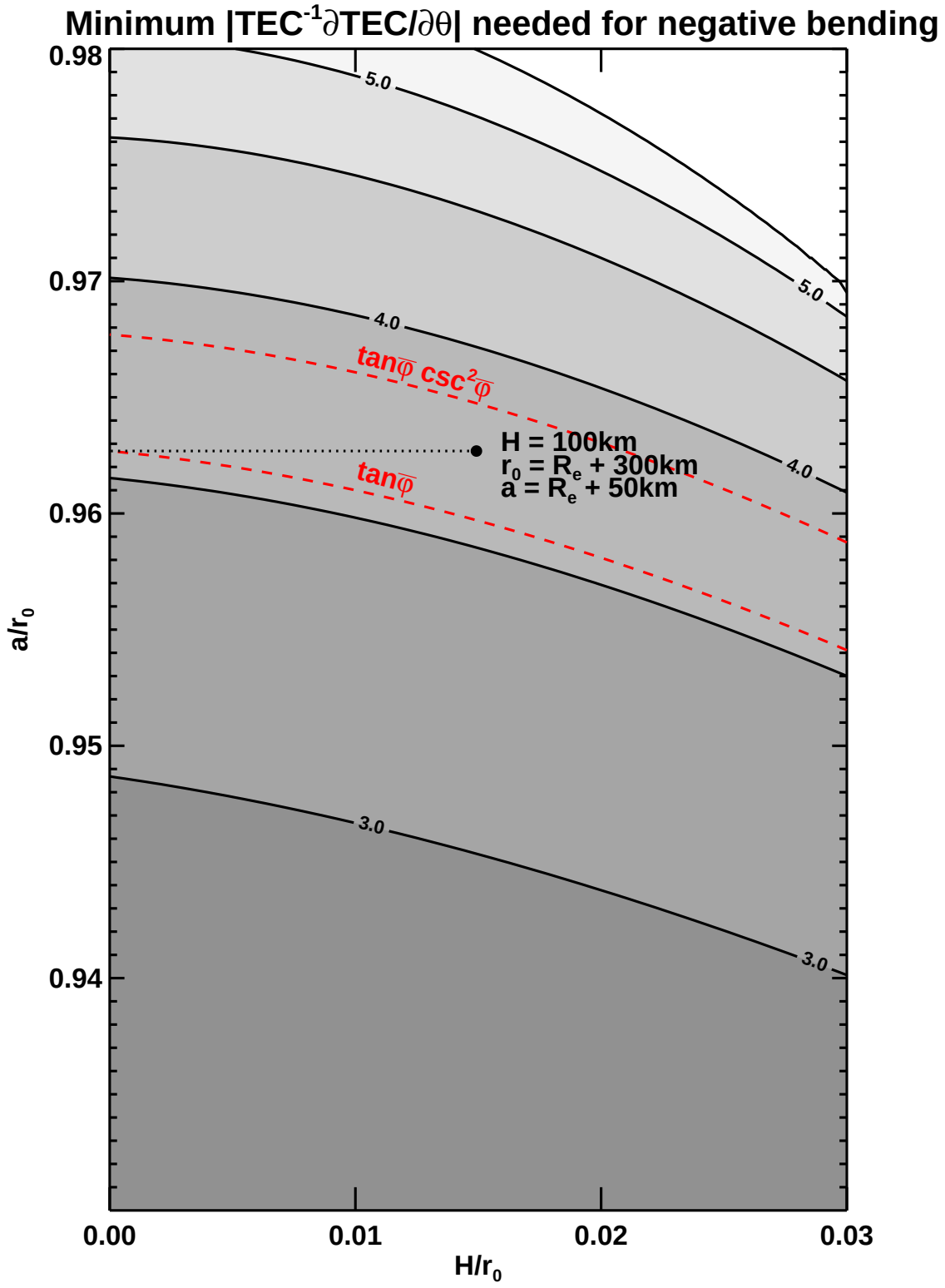

Figure 2.2: Minimum $|G/\delta_{PQ/2}|$ needed for negative bending (Eqn (2.30)) as a function of H/r_0 and a/r_0. Typical ionospheric values highlighted. Contours at $\tan\overline{\phi}$ (Eqn (2.31)) and $\tan\overline{\phi}\csc^2\overline{\phi}$ (Eqn (2.34))shown in red.

which would be negative if

$$G/\delta_{PQ/2} \leq \frac{-2(\tan\phi_0 - \tan\phi_2)}{(\tan\phi_0 + \tan\phi_2)\Delta\theta} \tag{2.33}$$

$$\rightarrow -\tan\overline{\phi}\csc^2\overline{\phi} \quad \text{as } H \rightarrow 0. \tag{2.34}$$

The difference between limits (2.34) and (2.31) is due to the $\cot\phi_0$ term in Eqn (2.30), which ultimately derives from $\phi_2' - \phi_2$ in Eqn (2.27). But in practice $\overline{\phi}$ is close to $\pi/2$, which makes the numerical difference between Eqns (2.31) and (2.34) rather small. *Hence, we can roughly estimate the extra bending induced by horizontal TEC gradients by simply accounting for the difference in refractive index at P and $Q(')$.*

This analysis suggests that to get significant difference from the 'baseline' positive bending induced by a homogeneous ionosphere, we would need significant changes in the TEC itself: the curvature of the ray path is unlikely to be sufficient. And this does indeed follow from the fact that $G\Delta\theta/\delta_{PQ/2} = \Delta\text{TEC}/\text{TEC}$, the fractional change in TEC over the ray path PQ'. Using $\Delta\theta \approx 2a(H/r_0)/\sqrt{r_0^2 - a^2}$ (~ 0.1) and $a \approx r_0 (\approx R_E)$, we finally deduce

$$\alpha' \leq 0 \implies |\Delta\text{TEC}/\text{TEC}| \geq H/(r_0 - a) \quad (\sim 0.4) \tag{2.35}$$

(All numerical estimates are for typical ionospheric parameters $H = 100$ km, $r_0 = R_E + 300$ km, $a = R_E + 50$ km.)

An equivalent expression to Eqn (2.35) has been derived independently (Syndergaard, 2012 [16]).

A 40% change in TEC over a distance $r_0\Delta\theta \sim 670$ km is rather large[2]. Fig 2.3a shows an instantaneous TEC map produced by CTIPe, the state of the art Coupled Thermosphere Ionosphere Plasmasphere Electrodynamics Model run by the US Space Weather Prediction Centre ([5]). Fig 2.3b shows the fractional change in TEC over 670 km. The resolution of the gridded data is 18° longitude by 2° latitude. The fractional change in TEC, $\Delta\text{TEC}/\text{TEC}$, is less than 40% over almost all of the domain, only exceeding it either side of the global maximum, or where the TEC itself is quite low. (The occultation plane would need to be aligned with this gradient to see the full effect, of course.) And this $\Delta\text{TEC}/\text{TEC}$ gives *zero* net bending. Significant negative bending, as negative as the unperturbed bending is positive, would require $\Delta\text{TEC}/\text{TEC}$ to be twice as large as this. And to avoid cancellation during the traversal of the other section of ionosphere on the other side of the tangent point, a similar refractivity gradient would need to appear, reversed, an angle $2\theta_0 \sim 30^o$ away. In other words, to obtain negative bending, the tangent point needs to be near a fairly strong minimum in the TEC. There are no such minima in Fig 2.3, although they are plausible.

In summary, we therefore conclude that horizontal TEC gradients *could* produce negative bending angles, but that, according to this model, they are likely to be rather uncommon.

[2]Large enough to stretch the small G approximation used in this analysis to breaking point, sadly. But we have still shown that small gradients are not sufficient to induce negative bending, even if the theory cannot give reliable estimates of the magnitude of gradients large enough to do so.

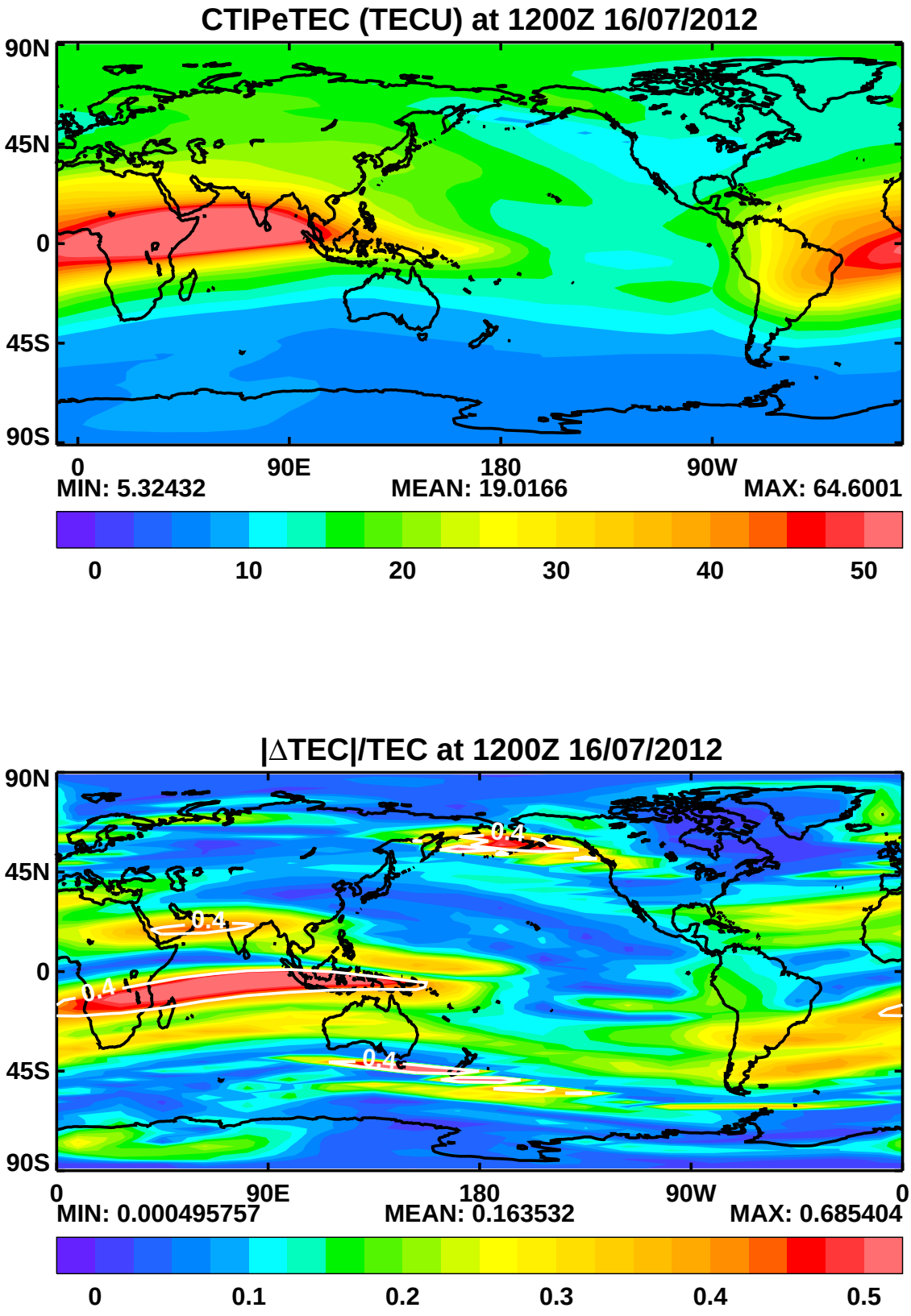

Figure 2.3: Example TEC distribution from the CTIPe model. Top: instantaneous value at 12Z 16/07/2012. Bottom: magnitude of fractional change in TEC over nominal ionospheric ray path of 670 km. 40% contour highlighted.

3 Sensitivity of L1 and L2 to the model ionosphere

In this Section we examine the sensitivity of the ionospheric bending angles to the shape and size of the ionospheric electron density profile, by calculating the L1 bending angle profiles, Eqn (2.4), for a variety of 1–D spherically symmetric model ionospheres. The models are briefly described before their solutions are compared.

3.1 Delta function ionosphere

A useful limiting case is obtained by considering a vanishingly thin ionosphere whose peak electron density increases in such a way that the TEC is finite. Such an electron density profile is given by[1]

$$n_e(r) = \mathrm{TEC}\,\delta(r - r_0). \tag{3.1}$$

Eqn (2.6) applies in this case and implies

$$\alpha(a) = \begin{cases} 2a(k_4/f^2)\mathrm{TEC}\, r_0(r_0^2 - a^2)^{-3/2} & \text{for } a - r_0 < 0 \\ 0 & \text{for } a - r_0 > 0 \end{cases} \tag{3.2}$$

Note the modest increase in bending angle with impact parameter a, until we approach r_0, the location of the delta function. (Contrast with the neutral bending angle which falls roughly *exponentially* with a.) The ionospheric bending angle is also proportional to TEC.

3.2 Slab ionosphere

We can get a feeling for the senitivity to the finite width of the ionosphere by modelling a uniform density slab ionosphere between $r_0 \pm H$:

$$n_e(r) = \frac{\mathrm{TEC}}{2H}\left(S(r - r_0 + H) - S(r - r_0 - H)\right). \tag{3.3}$$

where S is the unit step function ($S(x) = 1$ for $x > 0$, $S(x) = 0$ otherwise).

Eqn (2.4) applies in this case and implies

$$\alpha(a) = \begin{cases} 2a(k_4/f^2)(\mathrm{TEC}/2H)\left[\left((r_0 - H)^2 - a^2\right)^{-1/2} - \left((r_0 + H)^2 - a^2\right)^{-1/2}\right] & \text{for } a - r_0 < -H \\ -2a(k_4/f^2)(\mathrm{TEC}/2H)\left[\left((r_0 + H)^2 - a^2\right)^{-1/2}\right] & \text{for } |a - r_0| < H \\ 0 & \text{for } a - r_0 > H \end{cases} \tag{3.4}$$

Note that, correctly, the $a < r_0 + H$ solution is precisely twice as large as the 'entry point' bending angle calculated from first principles in Eqn (2.16).

[1] The theoretical objection to supposing an infinite electron density, as implied by a finite TEC spread over an ionosphere of vanishing thickness, alongside the $|n - 1| \ll 1$ approximation implicit in Eqn (2.3), is easily overcome. For, a typical TEC of 10^{17} m^{-3} dispersed over just a 100 m thick ionosphere still has, at RO frequencies, $n - 1 \sim 2 \times 10^{-3} \ll 1$. Since 100 m can be considered thin enough to be negligible in this problem, both approximations can hold at the same time.

3.3 Exponential ionosphere

We can get a feeling for the sensitivity to a long tail on the spaceward side of the ionosphere by considering a piecewise exponential electron density beyond r_0:

$$n_e(r) = \frac{\mathrm{TEC}}{2H} \exp(-u/2) S(r - r_0). \tag{3.5}$$

where $u = (r - r_0)/H$.

Eqn (2.4) now has the closed form solution (after approximating $\sqrt{r^2 - a^2} \approx \sqrt{r_0 + a}\sqrt{r - a}$),

$$\alpha(a) = \begin{cases} 2a(k_4/f^2)\frac{\mathrm{TEC}}{2H}\frac{1}{\sqrt{r_0^2 - a^2}}\left[1 - \sqrt{\pi l/2}\, e^{l/2}\ \mathrm{erfc}\ (\sqrt{l/2})\right] & \text{for } a - r_0 < 0 \\ 2a(k_4/f^2)\frac{\mathrm{TEC}}{2H}\frac{1}{\sqrt{r_0 + a}} \cdot -\sqrt{\pi/2H}\, e^{l/2} & \text{for } a - r_0 > 0 \end{cases} \tag{3.6}$$

where $l = (r_0 - a)/H$ and erfc is the usual complementary error function (eg Chap 7 Abromowitz and Stegun, 1965 [1]).

For the record, there is an analytical solution to the unfactorised Eqn (2.4) for $a > r_0$, namely

$$\alpha(a) = 2a(k_4/f^2)\frac{\mathrm{TEC}}{2H} \cdot -\frac{1}{2H} e^{r_0/2H} K_0(a/2H), \tag{3.7}$$

where K_0 is a modified Bessel function of the second kind (eg Chap 9 Abromowitz and Stegun, 1965 [1]).

3.4 Gaussian ionosphere

A smooth but symmetric variation in the electron density either side of the peak can be modelled by a Gaussian electron density distribution:

$$n_e(r) = \frac{\mathrm{TEC}}{2\sqrt{\pi}H} \exp(-u^2/4) \tag{3.8}$$

where $u = (r - r_0)/H$.

Eqn (2.4) cannot apparently be integrated in closed form for this electron density distribution, so we evaluate it numerically — a calculation which is aided by the substitution $x = a\cosh u$.

3.5 Chapman layer ionosphere

The asymmetric Chapman layer profile (Chapman, 1931 [4]) is often taken as a first order realistic model of the electron distribution in an ionospheric layer:

$$n_e(r) = \frac{\mathrm{TEC}}{\sqrt{2\pi e}H} \exp\left(\frac{1}{2}(1 - u - e^{-u})\right) \tag{3.9}$$

where $u = (r - r_0)/H$.

The Gaussian and exponential profiles have the same shape as the Chapman profile near its peak and over its long tail, respectively (if they have the same H). The calculation of the bending angle generated by a Chapman layer ionosphere is given in Sec 4. Here we calculate the bending by integrating Eqn (2.4) numerically.

3.6 Comparison

All five model electron density profiles are plotted in Fig 3.1a. They have been normalised to have the same TEC (10^{17} m^{-2}), peak height (300 km) and, except for the delta function, standard deviation about the peak (50 km). The resulting ionospheric bending angle profiles (for the L1 signal at $f \approx 1.6$ GHz) are shown in Fig 3.1b. They are clearly very different over the range of impact heights $a - R_E$ shown (0–600 km). All show a steady increase with a as the ionospheric peak is approached from below, followed by a decrease above the peak, except for those that vanish. This much follows from Eqn (2.4). However, for impact heights of interest in routine operational RO measurements, say 0–100 km, the bending angle profiles are much more similar. This is borne out by Fig 3.1c, which is a zooms in on the bottom 100 km of the bending angle profiles of Fig 3.1b. This figure shows that even at 100 km, the various bending angle profiles only differ by about 50% at most. This suggests that once the TEC, peak height and standard deviation of the electron density profile are fixed, there is little sensitivity to the precise shape. Fig 3.1d examines the sensitivity to doubling and halving TEC, r_0 and H in the slab model, Eqn (3.4), after adding a nominal 'neutral' bending angle profile as produced by a dry isothermal atmosphere at a temperature of 300 K and a scale height of 8 km. (This device shows that L1 and L2 are only really distinguishable from the neutral profile above about 50 km.) Here we do see some sensitivity, particulary to r_0. In this case $H = 87$ km, so reducing r_0 to 150 km brings the bottom edge of the slab down to about 63 km, which is why the bending angle profile diverges at that height. And siting the ionosphere twice as far away, by doubling $r_0 - R_E$ to 600 km, naturally reduces its impact on bending angles near the Earth. There is little sensitivity to halving H, which shows that we are close to the delta function limit in this instance. The variation with TEC is the straight proportionality embodied in Eqn (3.4).

In summary, the ionospheric bending angles are sensitive to the gross paramaters defining the ionosphere, but not to the subtleties of its electron density profile. We are therefore justified in choosing to study one particular density distribution whose TEC, peak height and width are variable. This is the subject to which we now turn.

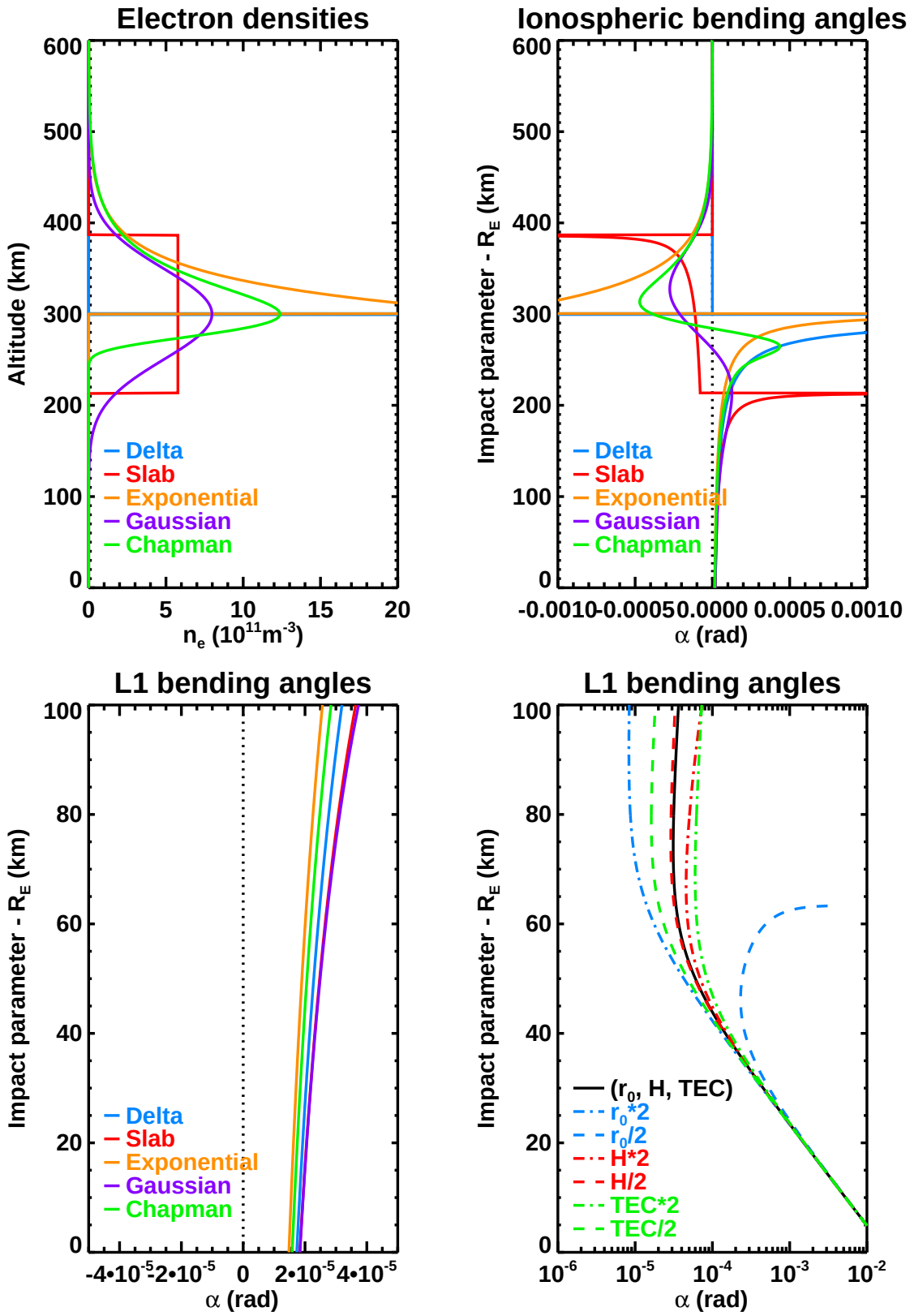

Figure 3.1: Sensitivity of bending angle to ionospheric parameters. Top left (a): Model electron density distributions. Top right (b): Ionospheric bending angle profiles. Bottom left (c): Ionospheric plus neutral bending angle profiles of (b), zoomed in on 0–100 km. Bottom right (d): Sensitivity to doubling and halving TEC, r_0 and H in the slab model, Eqn (3.4).

4 Bending induced by a Chapman layer ionosphere

The involved mathematical details of the evaluation of Eqn (2.4) when $n_e(x)$ is given by Eqn (3.9) are given in App A. The conclusion is that the bending angle α at impact parameter a, at frequency f, induced by a Chapman layer of thickness H, centred at r_0, having a total electron content TEC can be written as:

$$\alpha_i(a) = \alpha(a, f_i) = \frac{k_4}{f_i^2}\,\mathrm{TEC}\,\sqrt{\frac{2r_0^2a^2}{\pi H^3(r_0+a)^3}}\,Z\left(\frac{r_0-a}{H}\right) \tag{4.1}$$

where the dimensionless, order 1, function Z is defined by

$$Z(l) = \int_{-l}^{\infty} \frac{(e^{-3u/2} - e^{-u/2})\exp(-\frac{1}{2}e^{-u})}{\sqrt{u+l}}\,\mathrm{d}u. \tag{4.2}$$

The function Z describes most of the variation of bending angle with height, since the other factors in Eqn (4.1) only vary slowly over the range of impact parameters a of interest. Crucially, Z depends only on the parameter $l = (r_0 - a)/H$, the distance from the peak of the Chapman layer expressed in widths of the layer. For practical RO applications, $2 \lesssim l \lesssim 10$.

Various methods of calculating $Z(l)$ are described in App A. For practical purposes in the rest of this paper we settle on the Padé approximation Eqn (A.27) detailed in Sec A.5, as it is much quicker to evaluate than direct numerical integration, and accurate enough (within 2.2%).

$Z(l)$ is sketched in Fig A.1, as is the fractional error in the Padé approximation to it. The biggest error in the region not shown is about 1.8% at $l \approx 20$.

5 Theoretical feasibility of making a retrieval using L1 and L2 directly

Given that we can calculate the bending from a single Chapman layer according to Eqns (4.2) and (A.27), it is reasonable to ask whether it is worth doing so. Might it give better retrievals than using the ionospherically corrected neutral bending angle, as we do now? And even if the L2 signal dropped out completely, might the L1 signal alone be able to generate a useful retrieval? To throw some light on these questions we have carried out some one-dimensional variational retrieval ('1D–Var') experiments on a very simple 0-D model of an atmosphere, which comprises a single Chapman layer of ionospheric parameters TEC, H, r_0 above a dry, uniform temperature (=T) atmosphere at surface pressure $p*$. (A constant *absolute* temperature is not such a poor theoretical approximation.) The bending angles in this simple model atmosphere are as follows:

$$\alpha_{L1,2}(a) = \alpha_n(a) + \alpha_{i1,2}(a) \tag{5.1}$$

where

$$\alpha_n(a) = \frac{k_1 p*}{T}\sqrt{\frac{2\pi g a}{RT}}\exp\left(-\frac{g(a-R_E)}{RT}\right) \tag{5.2}$$

is the neutral bending, and (after rewriting Eqn (4.1) in terms of the peak electron density of the Chapman layer, $n_e^{max} = \mathrm{TEC}/\sqrt{2\pi e}H$),

$$\alpha_{i1,2}(a) = (k_4/f_{L1,2}^2)n_e^{max}\sqrt{\frac{4er_0^2a^2}{H(r_0+a)^3}}\,Z\left(\frac{r_0-a}{H}\right) \tag{5.3}$$

is the ionospheric bending at the two frequencies L1 and L2.

There are five elements in the state vector $\mathbf{x} = \{T, p*, n_e^{max}, r_0, H\}$, and the analytic form of the forward model $\mathbf{H}$ allows easy generation of the tangent linear matrix $\mathbf{K} = \partial\mathbf{H}/\partial\mathbf{x}$, which is needed in the cost function minimisation. We use n_e^{max} rather than TEC as it is probably less correlated with H, and all elements of the state vector will be assumed to be uncorrelated. To keep the number of terms in each half of the cost function (Eqn (5.4) below) approximately the same, we calculate bending angles on just 5 levels.

We start by assuming a true state vector $\mathbf{t}$. This is then randomly perturbed by assuming that the actual T, $p*$ etc are Normally distributed around the true value with the standard deviations shown in Table 5.1. Each such perturbed state defines a background $\mathbf{b}$. Similarly, we forward model $\mathbf{t}$ using Eqns (5.1)–(5.3) to generate α_{L1} and α_{L2}. These are also randomly perturbed assuming Gaussian distributions having standard deviations that are the given functions of the actual bending angles also shown in Table 5.1. These make up the pseudo-observations $\mathbf{y}$. Finally, we pass the set through a Levenberg-Marquardt minimisation of the usual 1D–Var cost function (eg Healy and Eyre, 2000 [9])

$$J(\mathbf{x}) = 1/2(\mathbf{x}-\mathbf{b})^T\mathbf{B}^{-1}(\mathbf{x}-\mathbf{b}) + 1/2(\mathbf{y}-\mathbf{H}(\mathbf{x}))^T\mathbf{O}^{-1}(\mathbf{y}-\mathbf{H}(\mathbf{x})) \tag{5.4}$$

to give the analysed state (or retrieval) $\mathbf{a} = \arg(\min J)$. Here $\mathbf{B}$ and $\mathbf{O}$ are the covariance matrices constructed from the same errors that were used to construct $\mathbf{b}$ and $\mathbf{y}$. Since we are assuming uncorrelated errors in the state vector elements, and observations, both matrices are diagonal.

We repeat the retrieval 10000 times using different pseudo-backgrounds and pseudo-observations, all based on the same true state, the parameters of which are listed in Table 5.1. We compare the statistics of $\mathbf{a}-\mathbf{t}$ and $\mathbf{b}-\mathbf{t}$ to assess the impact of assimilating the observations.

Toy model parameters		
Field	True value	Error
T	250 K	2 K
$p*$	1000 hPa	10 hPa
n_e^{max}	3.0×10^{11} m^{-3}	1.5×10^{11} m^{-3}
r_0	R_E+300 km	50 km
H	75 km	25 km
α_n	Eqn (5.2)	1% true
α_{i1}	Eqn (5.3)	1% true
α_{i2}	Eqn (5.3)	1% true
α_{LC}	Eqn (5.5)	Eqn (5.6)

Table 5.1: Specification of true state and background and observational errors.

5.1 Control: retrieval based on ionospherically corrected bending angle LC

This is a simplified version of current operational NWP procedure. The ionospherically corrected neutral bending angle signal is estimated by simple elimination of α_1 and α_2 to be

$$\alpha_{LC} = \frac{\alpha_{L1} f_{L1}^2 - \alpha_{L2} f_{L2}^2}{f_{L1}^2 - f_{L2}^2} \tag{5.5}$$

The error on α_{LC}, assuming the errors on α_{L1} and α_{L2} to be uncorrelated (which they are by design in this model problem), is given by

$$\sigma_{LC}^2 = \sigma_{i1}^2 \left(\frac{f_{L1}^2}{f_{L1}^2 - f_{L2}^2} \right)^2 + \sigma_{i2}^2 \left(\frac{f_{L2}^2}{f_{L1}^2 - f_{L2}^2} \right)^2 \tag{5.6}$$

This expression implies that the minimum error on α_{LC} is two or three times that on α_{L2} and α_{L1} (respectively). The errors on α_{LC} are larger because it is the difference between two similarly sized quantities. The hope is that by using the better (ie lower error, and much lower fractional error) L1 and L2 signals directly, we might obtain a better retrieval than at present. The forward model $\mathbf{H}$ in Eqn (5.4) is given by $\mathbf{H}(\mathbf{x}) = [\alpha_n]$: there is clearly no sensitivity to n_e^{max}, r_0 or H.

Fig 5.1 shows an example of the convergence of the state during the minimisation of the cost function. In this case the analysed temperature is further from the truth than the background is. The reverse is true for the surface pressure. There is obviously no change in n_e^{max}, r_0 or H in this case. The cost function at analysis is slightly smaller than it is at background.

Fig 5.2 shows histograms of $\mathbf{b}-\mathbf{t}$ and $\mathbf{a}-\mathbf{t}$. They are both centred on $\mathbf{0}$: the first by design; the second suggesting that linear theory (in which it would hold) is approximately true here. The analysed T and $p*$ distributions have a smaller spread than the background distributions — in other words, the observations have tightened up the retrievals by adding extra information to the prior distribution. This is borne out by the statistics. The dashed curves are Gaussian distributions with widths given by (the square roots of the diagonal elements of) the background covariance matrix $\mathbf{B}$ and the analysis covariance matrix $\mathbf{A} = (\mathbf{B}^{-1} + \mathbf{K}^T \mathbf{O}^{-1} \mathbf{K})^{-1}$. (These numbers are printed on the plots.) Clearly the latter are smaller than the former. A more quantitative comparison appears in Sec 5.5.

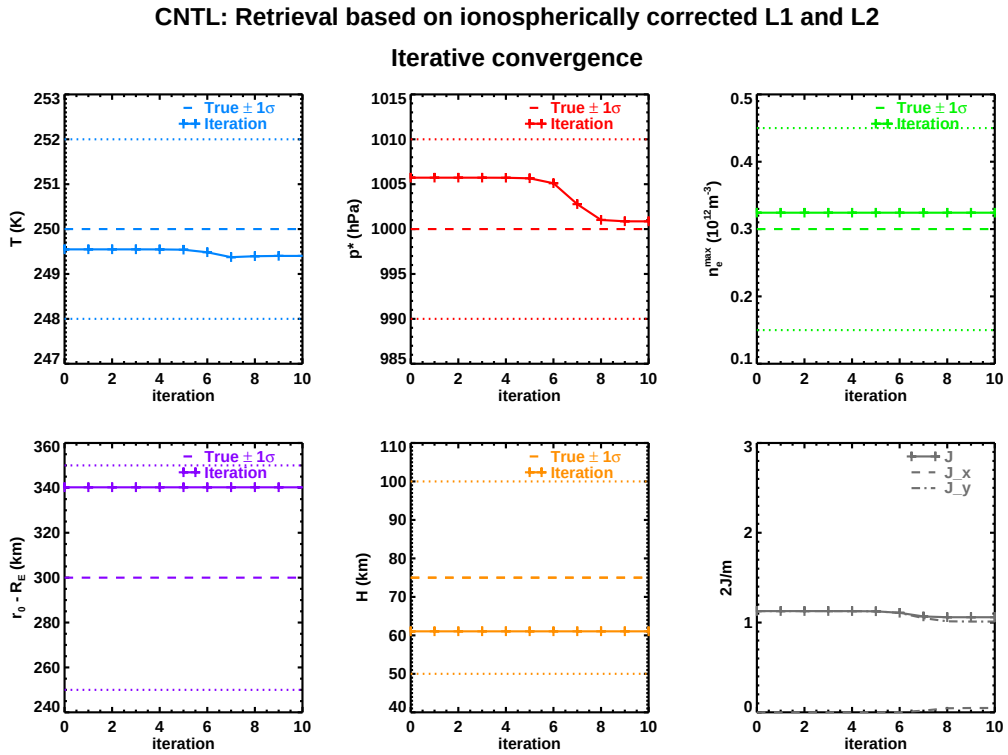

Figure 5.1: Example of iterative convergence of T, $p*$, n_e^{max}, r_0, H and $2J/m$ in control experiment.

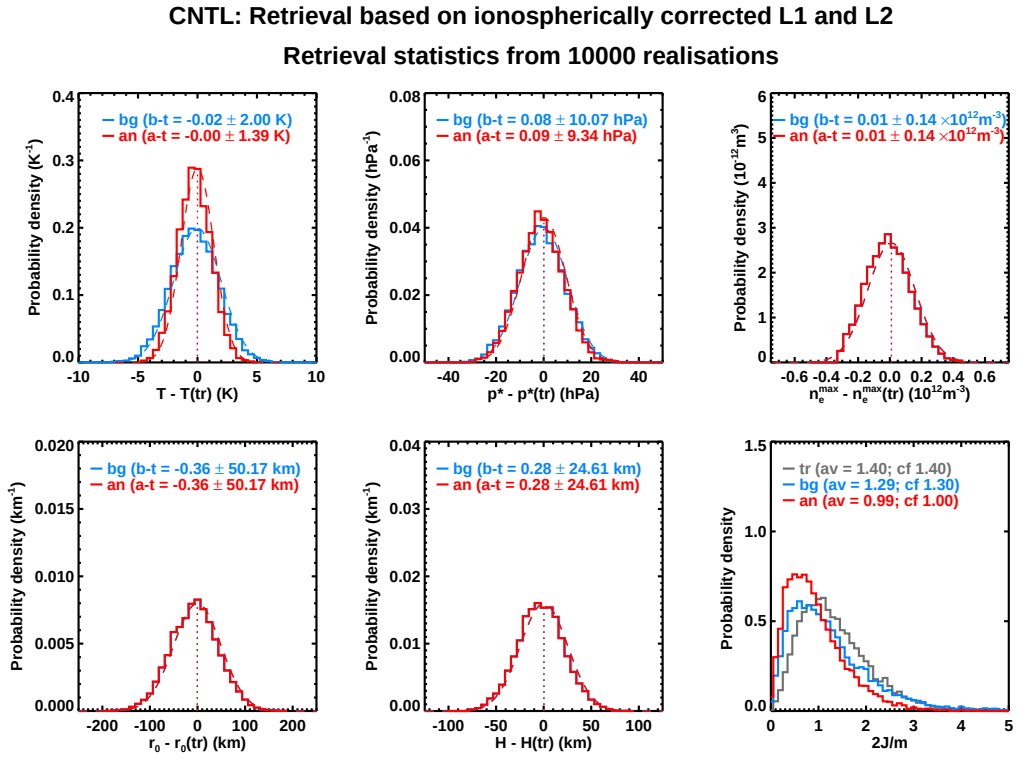

Figure 5.2: Histograms of $\mathbf{b}-\mathbf{t}$ (blue) and $\mathbf{a}-\mathbf{t}$ (red) for control experiment ensemble.

5.2 Test 1: retrieval based on L1 and L2 bending angles

In this experiment we use both α_{L1} and α_{L2}, which makes $\mathbf{y}$ twice as long as in the control. The forward model is given by $\mathbf{H}(\mathbf{x}) = [\alpha_n + \alpha_{i1}, \alpha_n + \alpha_{i2}]$, and there is sensitivity to all elements of $\mathbf{x}$.

Fig 5.3 shows the convergence of the state during the minimisation of the cost function. The key difference from the control experiment is of course the variation of n_e^{max}, r_0 and H, on which both L1 and L2 depend. In this particular case the analysis brings all five background state variables nearer to the truth. The cost function at analysis is much (700 times) smaller than it is initially.

Fig 5.4 shows histograms of $\mathbf{a} - \mathbf{t}$ and $\mathbf{b} - \mathbf{t}$. The analysed T, $p*$, n_e^{max}, r_0 and H all show smaller mean square deviations from the truth than their corresponding backgrounds.

We note that the 1D–Var retrieval has introduced a mean shift in the retrieved r_0 of about -9 km. This shows that non-linear terms in the forward model are having an impact.

Interestingly, the retrieved T and $p*$ are significantly better (smaller variance) than they are in the control experiment. This is a very tentative suggestion that we may get better retrievals of the atmospheric parameters — the things in which we are really interested — by modelling L1 and L2 directly, rather than by modelling their ionospherically corrected combination. We suggest that this is due to the smaller errors on α_{L1} and α_{L2} than on their linear combination α_{LC}. This conclusion is, however, strongly dependent on the rather arbitrary errors attached to the background parameters and to L1 and L2.

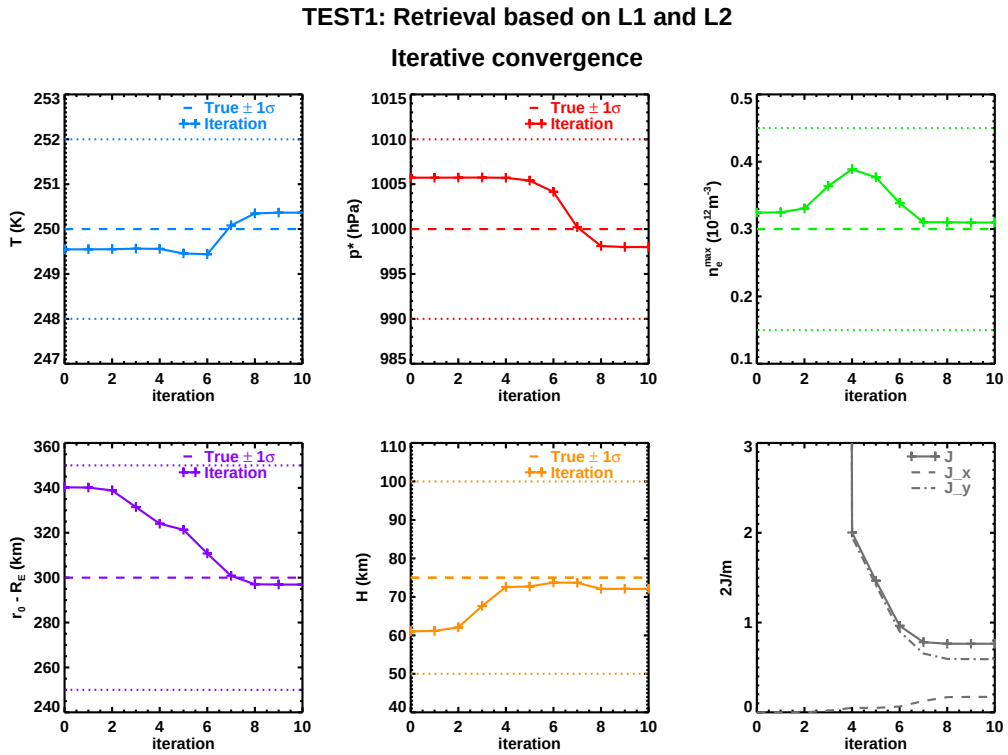

Figure 5.3: Example of iterative convergence of T, $p*$, n_e^{max}, r_0, H and $2J/m$ in first test experiment.

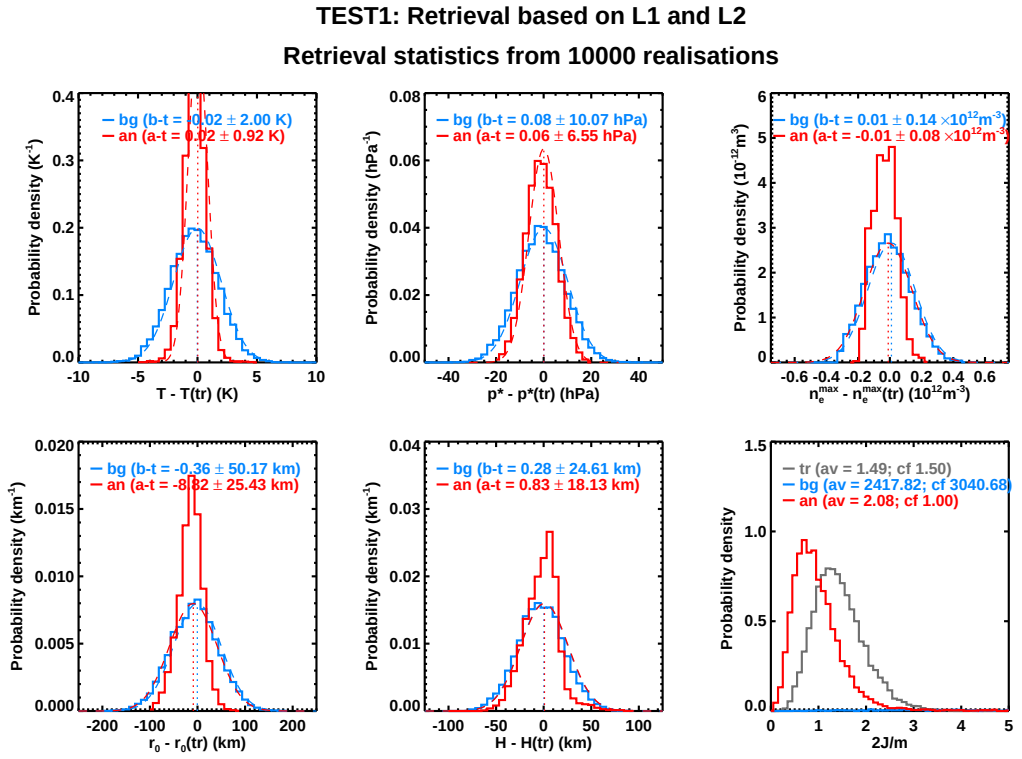

Figure 5.4: Histograms of $\mathbf{b}-\mathbf{t}$ (blue) and $\mathbf{a}-\mathbf{t}$ (red) for first test experiment ensemble.

5.3 Test 2: retrieval based on L1 bending angle only

In this experiment we use just α_{L1}, so $\mathbf{y}$ has the same length as in the control. The forward model is given by $\mathbf{H}(\mathbf{x}) = [\alpha_n + \alpha_{i1}]$, so there is sensitivity to all elements of $\mathbf{y}$. This is the limiting case of possible interest: the L2 signal is completely missing.

Fig 5.5 shows the convergence of the state during the minimisation of the cost function. Again, in this particular case the analysis brings all five background state variables nearer to the truth. The cost function at analysis is much (800 times) smaller than it is at background. Despite only having half the number of observations of the first test, the retrieval is remarkably similar. This suggests that a decent retrieval may just be possible using L1 alone. Closer scrutiny of the distributions of $\mathbf{a}-\mathbf{t}$ and $\mathbf{b}-\mathbf{t}$ shown in Fig 5.6 show that in fact the variances in Test 2 are larger than those of Test 1, but that, for T and $p*$, they are still smaller than in the control experiment. And, as for Test1, a (similar) bias has appeared in the analysed r_0.

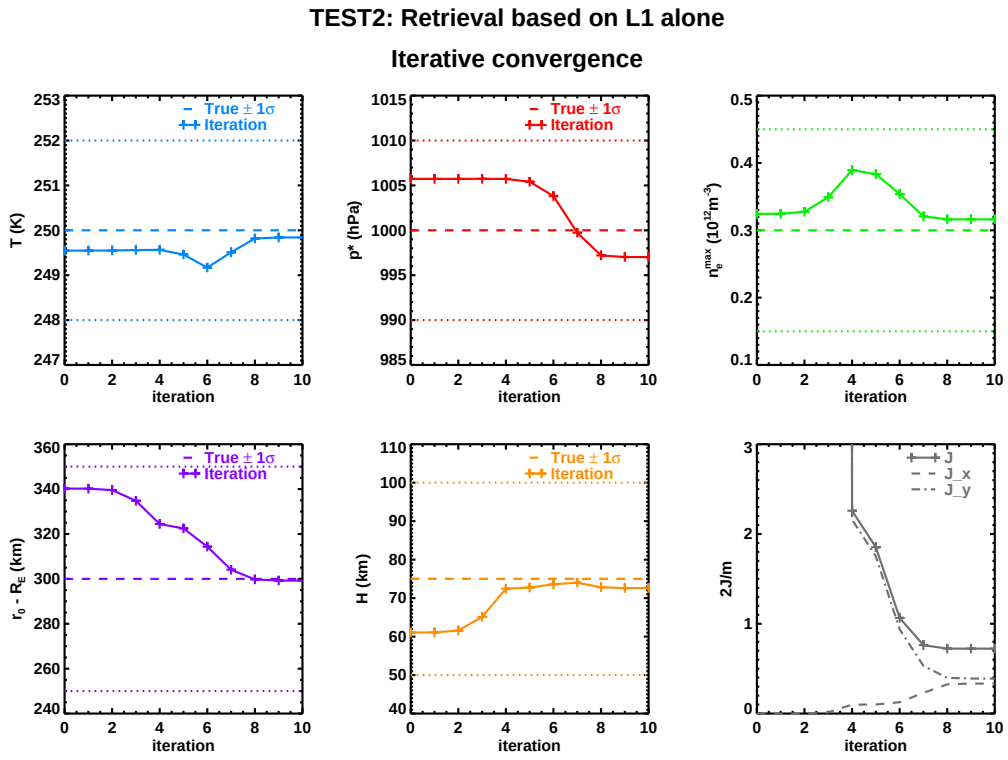

Figure 5.5: Example of iterative convergence of T, $p*$, n_e^{max}, r_0, H and $2J/m$ in second test experiment.

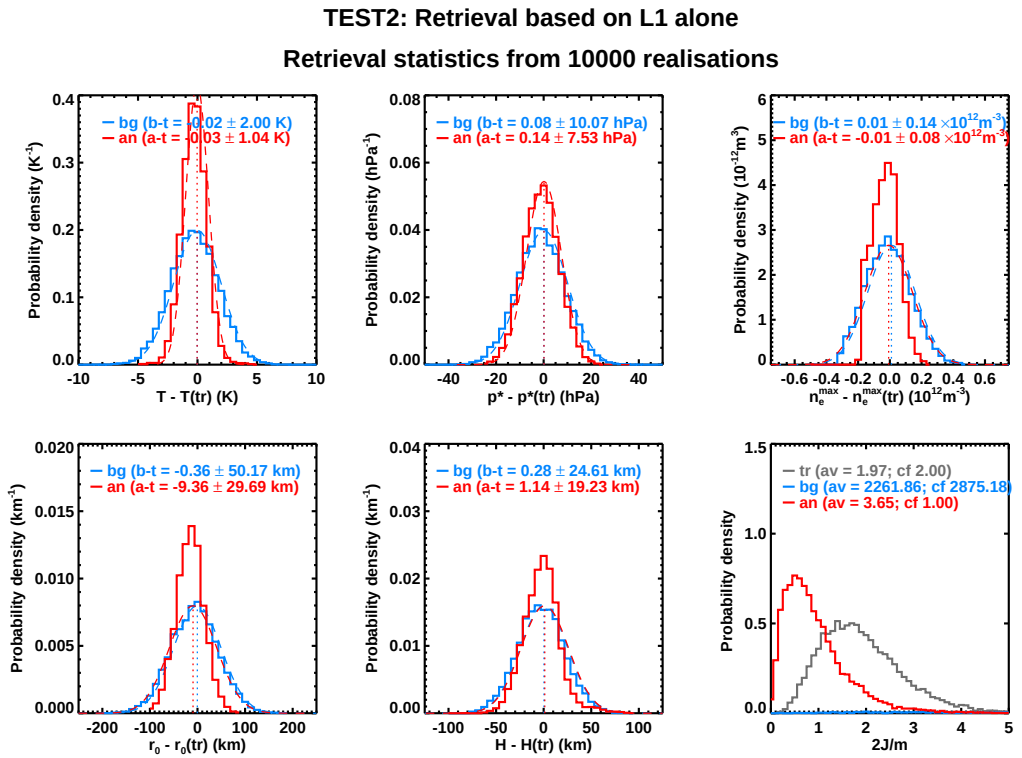

Figure 5.6: Histograms of $\mathbf{b}-\mathbf{t}$ (blue) and $\mathbf{a}-\mathbf{t}$ (red) for second test experiment ensemble.

5.4 Test 3: retrieval using L1 as a proxy for LC

Another way of coping with the loss of the L2 bending angle is to simply pretend that L1 is the neutral bending angle, and to increase the errors in the 1D–Var retrieval system to account for the necessarily large difference between the two at height. This is what we do in this experiment, in which the observation vector $\mathbf{y} = \alpha_{L1}$, and the forward model is given by $\mathbf{H}(\mathbf{x}) = [\alpha_n]$. There is therefore no sensitivity to the ionospheric elements of the state vector $\mathbf{x}$.

Since the errors on LC and L1 are uncorrelated in this experiment, we would expect the variance of the error on $\alpha_{L1} - \alpha_n$ to be given by

$$\sigma^2_{LC-n} = \sigma^2_{L1} + \sigma^2_n \tag{5.7}$$

In fact, because the neutral forward model cannot hope to model the 'flattening' of the L1 bending angle with height, we find that these errors need to be inflated fivefold in order to get any kind of sensible 1D–Var retrieval. Using an inflation factor of less than five gives rise to enormous cost functions and very significant biases in the analysed model parameters; inflating by factors of greater than five leads to more modest cost functions but hardly any change in the state variables from their background values — in other words, it nullifies the effect of the observations altogether.

Fig 5.7 shows the convergence of the state during the minimisation of the cost function. The very high initial cost function (note the different scale on the y-axis) is slightly reduced by the changes in T and $p*$. More interesting are the histograms of the analyses and backgrounds shown in Fig 5.8. The retrieval has introduced a significant bias of 1.2 K into the temperature T and a less significant one of 1.5 hPa into $p*$. Both evidently increase the neutral bending angle as calculated with Eqn (5.2). The mean $2J/m$ (note the different scale on the x-axis to that in the other runs) is also about ten times larger than expected. Both indicate (understandable) problems in retrieving L1 bending angles with a neutral atmosphere forward model.

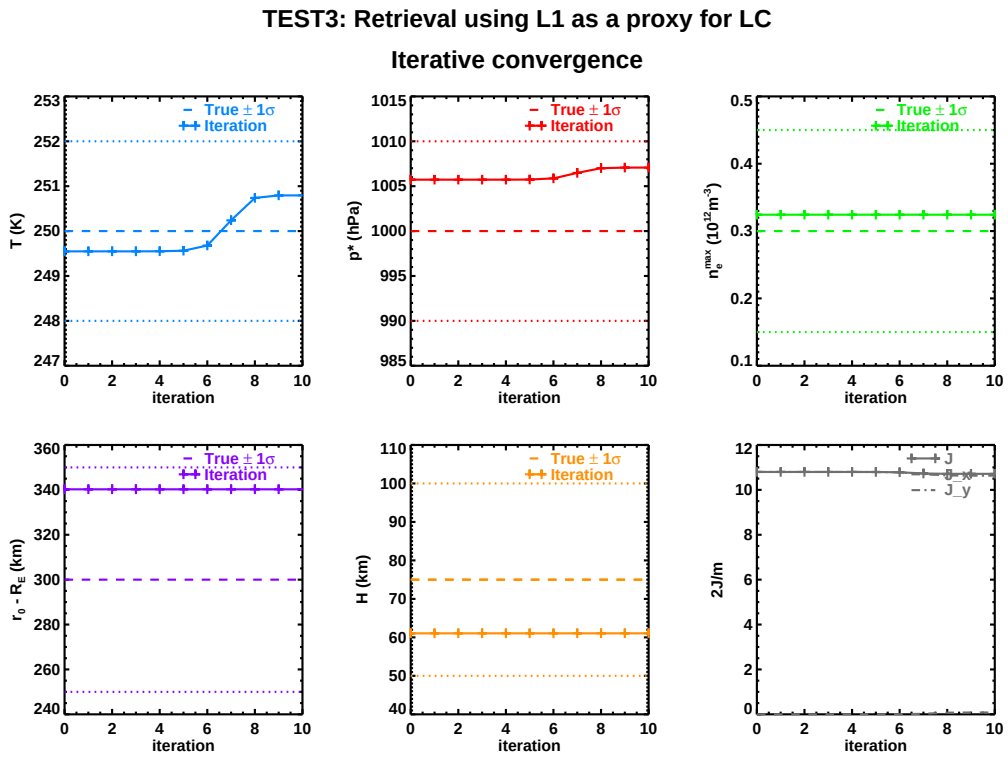

Figure 5.7: Example of iterative convergence of T, $p*$, n_e^{max}, r_0, H and $2J/m$ in third test experiment.

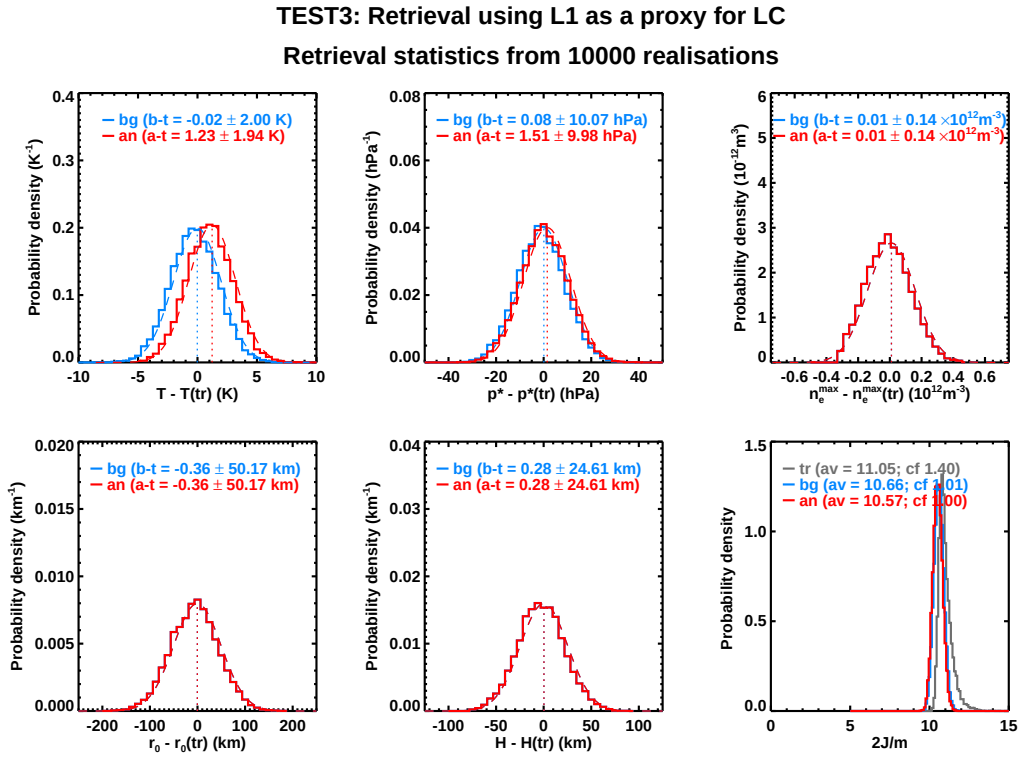

Figure 5.8: Histograms of $\mathbf{b}-\mathbf{t}$ (blue) and $\mathbf{a}-\mathbf{t}$ (red) for third test experiment ensemble.

5.5 Comparison

Table 5.2 lists, for all four experiments, $||\mathbf{a}-\mathbf{t}||_2/||\mathbf{b}-\mathbf{t}||_2$, the reduction in the standard deviation of the state variables arising from the addition of observational information to the prior state during the retrieval procedure. It also lists the mean value of $2J/m$ for the analyses. (Recall that the expectation value of this is unity for linear forwrd models.) It can be seen that Test 1, which has twice as many observations as the Control experiment, gives better retrievals according to this measure. This result is, however, strongly dependent on the errors and background values, which are open to some question. Less contentious, because the systems are identical apart from the number of observations, is the conclusion that Test 2, which uses the L1 bending angles alone, is nearly as good as Test 1, which uses both L1 and L2. Also suggestive is the result that Test 3, in which L1 serves a direct proxy for LC, gives the least reduction in the state vector variance of all, as well as incurring very large cost functions.

$\|\|\mathbf{a}-\mathbf{t}\|\|_2/\|\|\mathbf{b}-\mathbf{t}\|\|_2$, and $\overline{2J(an)/m}$, in model retrieval system						
Experiment	T	$p*$	n_e^{max}	r_0	H	$2J/m$
Cntl	0.695	0.928	1	1	1	0.99
Test 1	0.460	0.650	0.557	0.507*	0.737	2.08
Test 2	0.520	0.748	0.600	0.592*	0.781	3.65
Test 3	0.970*	0.991*	1	1	1	10.57

Table 5.2: $||\mathbf{a}-\mathbf{t}||_2/||\mathbf{b}-\mathbf{t}||_2$, and $\overline{2J(an)/m}$, for state elements in model retrieval system. *Subject to some bias in the analysis.

These simple idealised experiments suggest, very tentatively, that direct modelling of a single Chapman layer ionosphere might give better retrievals than the ionospherically corrected linear combination of L1 and L2 used presently, and that this result may still hold even if L2 is unavailable. It certainly appears preferable to simply using L1 as a proxy for LC. Whether the same is true with real RO data remains to be seen. It would require running a series of VAR trials with these changes in the forward model. The impact on the surface pressure and temperature could then be assessed properly. This work is planned. A natural first step in this direction would be to examine whether observed bending angles can be even approximately modelled by means of a spherically symmetric Chapman layer ionosphere. This is the subject of the next Section.

6 Fitting GRAS L1 – L2 data

Sec 5 has suggested that there may be advantages to modelling the L1 and L2 bending angles separately, by means of a Chapman layer ionosphere. To test this hypothesis further, the L1 and L2 occultations from the GRAS[1] instrument on Metop-A[2] for 5 consecutive days in June 2012 were downloaded from the ROM SAF website (ROM SAF 2014, [14]) — around 3500 occultations in total. For each profile, the neutrally corrected signal L1 – L2 was calculated, truncated below 30 km (to focus on the ionospherically dominated bending angles), and fitted to a Chapman layer bending angle profile thus:

$$\alpha_{L1}(a) - \alpha_{L2}(a) = k_4(f_{L1}^{-2} - f_{L2}^{-2}) n_e^{max} \sqrt{\frac{4er_0^2a^2}{H(r_0+a)^3}}\, Z\left(\frac{r_0-a}{H}\right), \tag{6.1}$$

as found by using Eqns (5.1) and (5.3). When it converges successfully, the (Levenberg-Marquardt) fitting routine returns estimates of TEC, r_0 and H. An example of a successful retrieval is shown in Fig 6.1. Reasonable ionospheric parameters are returned from a close fit. An example of an unsuccessful retrieval is shown in Fig 6.2. In the second case, L1 – L2 is positive, which, in this framework, implies that $Z(l) < 0$. Moreover, |L1 – L2| is *reducing* with height, which puts it in the top third of the $Z(l)$ curve — well above the ionospheric peak height. This can be ruled out on physical grounds. The reason for this and other L1 > L2 retrievals is under investigation. Horizontal gradients of electron density, which violate the spherical symmetry approximation, have been suggested as one possibility, but the analysis of Sec 2.2 suggests this is unlikely to be sufficiently strong or common enough to explain the abundance of such 'anomalous' profiles.

When these and other similarly unphysical least square fit retrievals (those with TEC < 0 or > 100 TECU, those with r_0 or H < 0 or > 1000 km, or those whose sum of squared residuals exceeds 10 times the number of points being fitted) are ruled out, about 2000 'good' profiles, out of the original set of 3500, remain. When these are put on a 400 km resolution grid, which is about the same horizontal resolution as a Radio Occultation measurement, the TEC map shown in Fig 6.3 is produced. Although there is clearly a lot of noise in the retrievals, the distribution is roughly correct: peaking in the tropics at around 25 TECU in the zonal mean, and arguably a little smaller in the southern hemisphere. An independent analysis of the global TEC in the middle of this 5-day period is shown in Fig 6.4 (Bureau of Meteorology, 2014 [3]). The two fields are in broad agreement, especially when the diurnal variation of TEC is considered. For what it is worth, the retrieved Chapman layer peak height r_0 and thickness H peak strongly in the southern hemisphere — see Figs 6.5 and 6.6. There is some evidence that the peak of the ionosphere lifts as the winter pole is approached (eg Zhang and Holt, 2007 [18]).

The results of this section suggest that, when L1 and L2 can be fitted to a single Chapman layer, the resulting estimates of the ionospheric parameters are sensible. This lends a little confidence to the method. They should not, however, be viewed as *measurements* of the ionosphere. Many different model ionospheres could produce the given bending angles: this method simply retrieves the defining characteristics of the Chapman layer ionosphere that would do so — when it can.

Interpolating or extrapolating L2 from L1 – L2 differences is the current operational procedure when the L2 signal drops out. This analysis here suggests that a physically based interpolation method based on Chapman layer bending angle profiles may be no worse than this. Where L1 – L2 cannot be fitted by Eqn (6.1), the current method could be employed.

[1] Global Navigation Satellite System Receiver for Atmospheric Sounding (ie an RO receiver).
[2] EUMETSAT's operational polar orbiting meteorological satellite, launched in 2006.

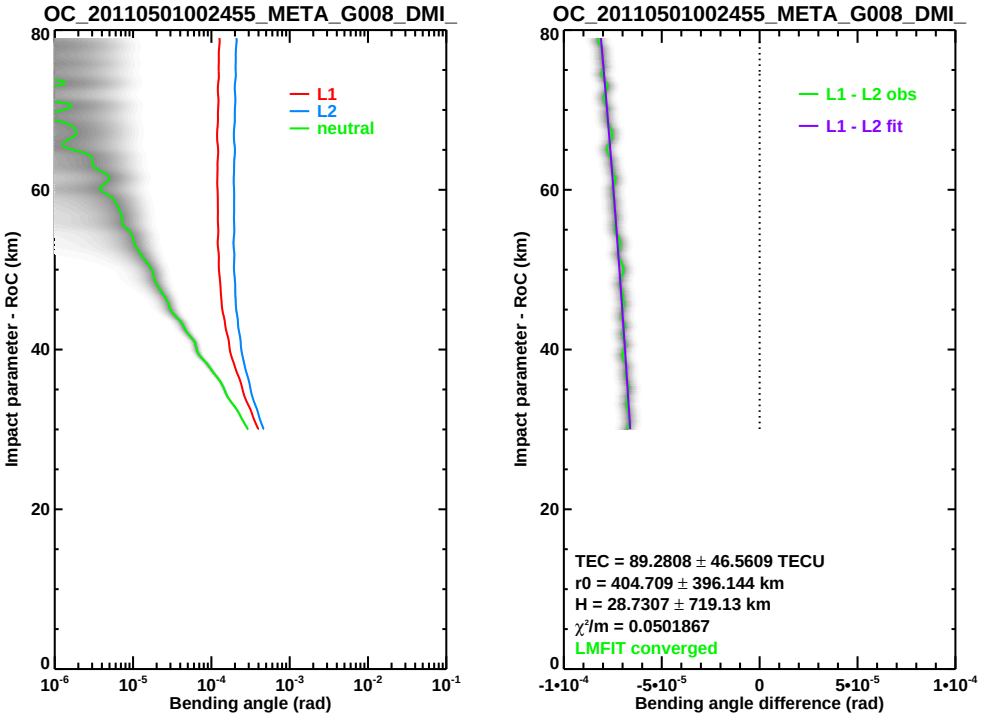

Figure 6.1: Example of a successful and physically reasonable least squares fit of Eqn (6.1) to neutrally corrected RO signal L1 – L2.

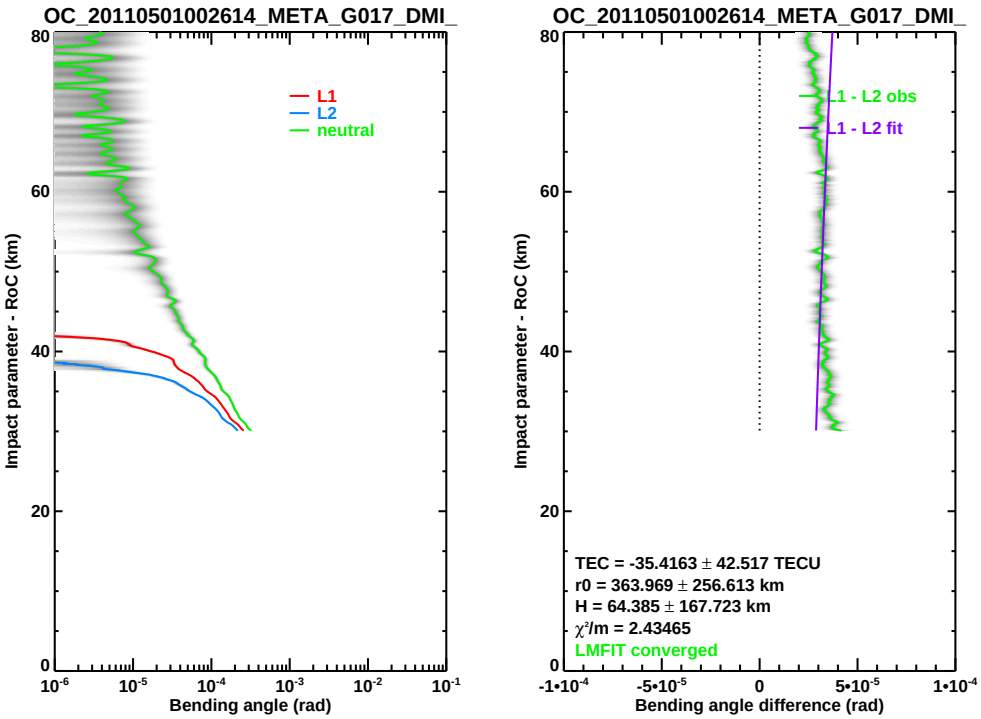

Figure 6.2: Example of a successful but physically dubious least squares fit of Eqn (6.1) to neutrally corrected RO signal L1 – L2.

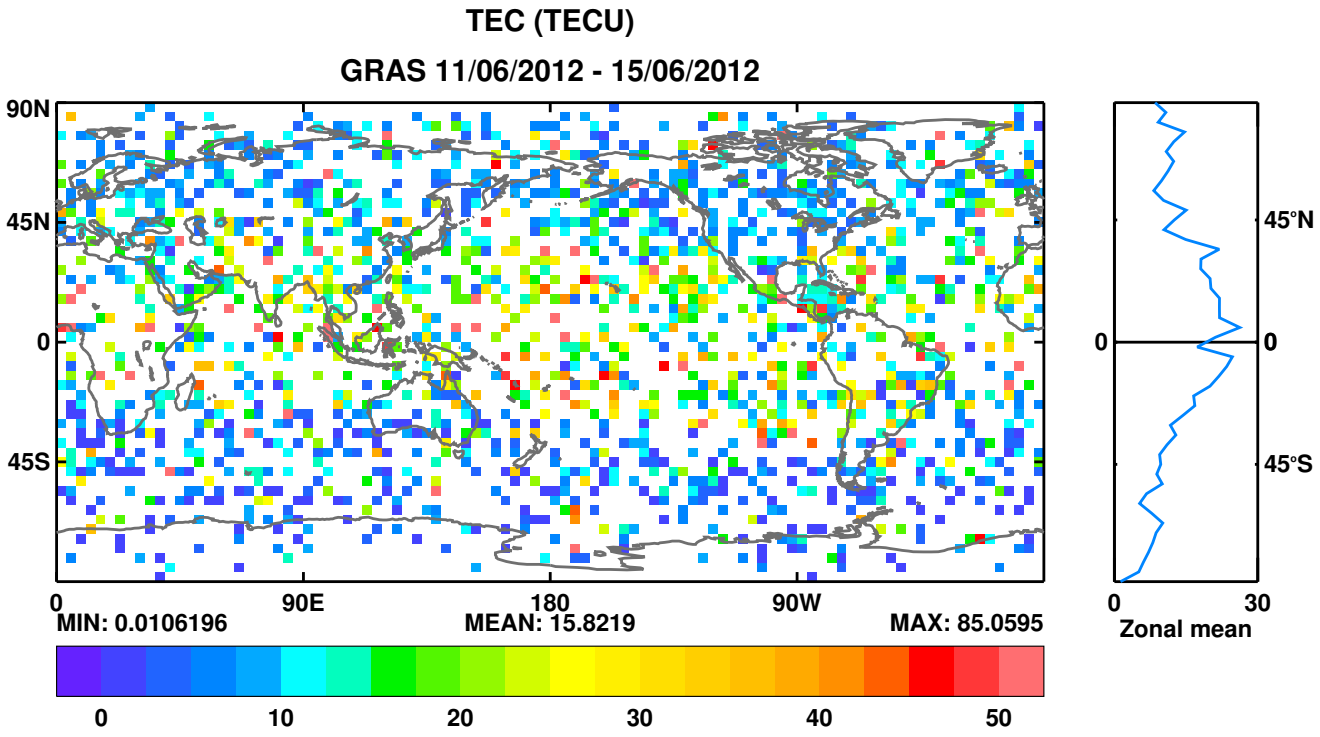

Figure 6.3: Global maps of retrieved Chapman layer total electron content TEC from 2000 'good' least squares fits to the GRAS L1 – L2 bending angles between 11th and 15th June 2012.

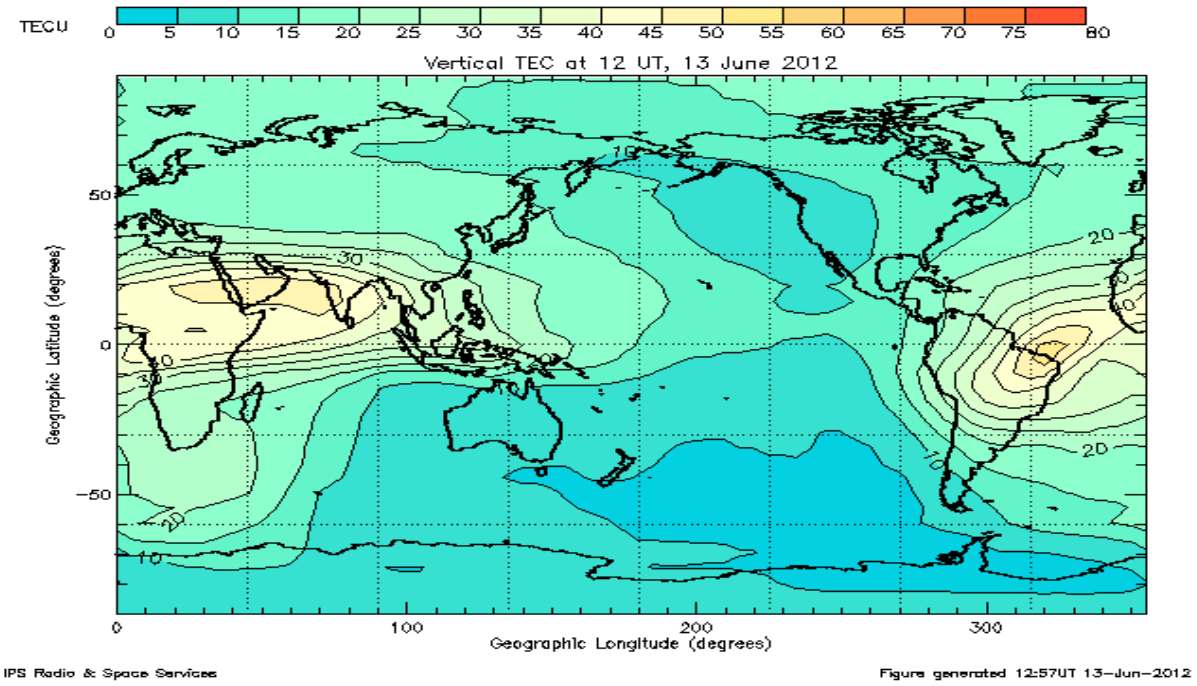

Figure 6.4: TEC analysis for 12Z 13th June 2012 produced by IPS ([3]). This is derived from IRI model background driven by ionosonde data, and GNSS phase delay data assuming a delta-function ionosphere.

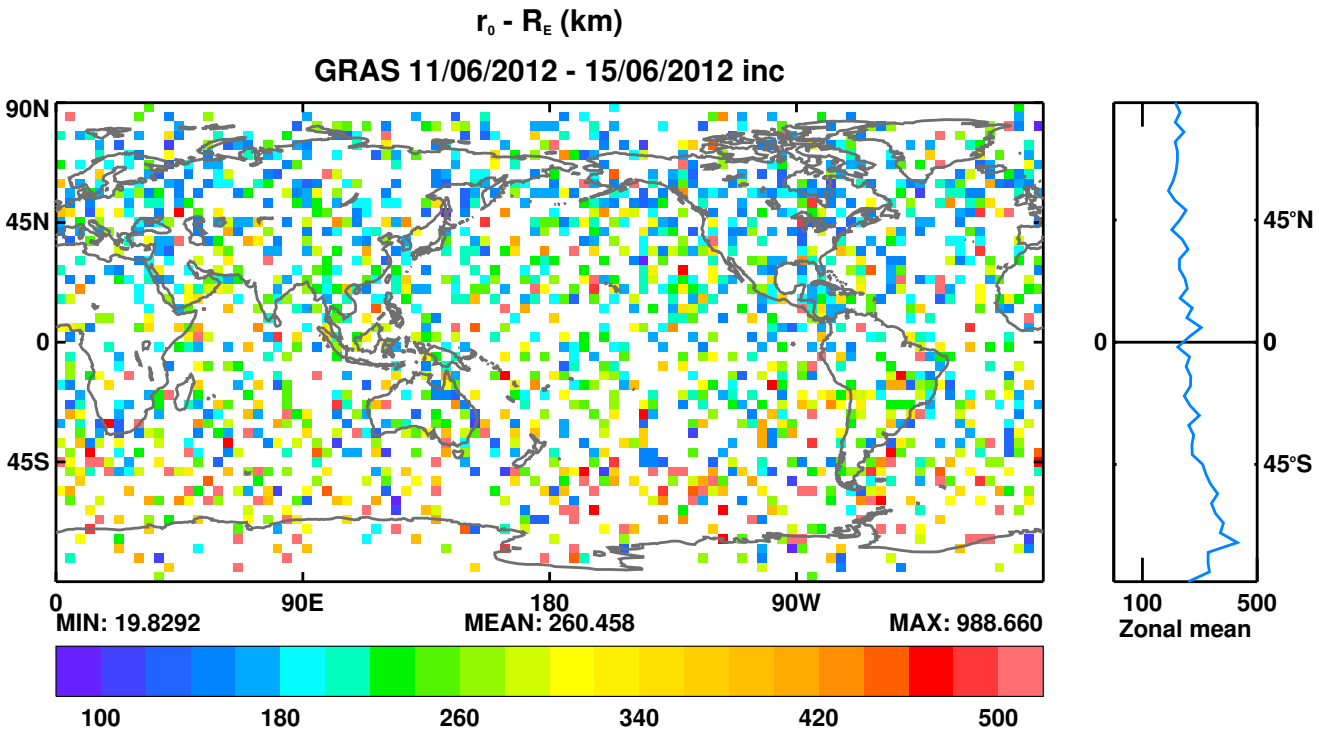

Figure 6.5: Global maps of retrieved Chapman layer peak height r_0 from 2000 'good' least squares fits to the GRAS L1 – L2 bending angles between 11th and 15th June 2012.

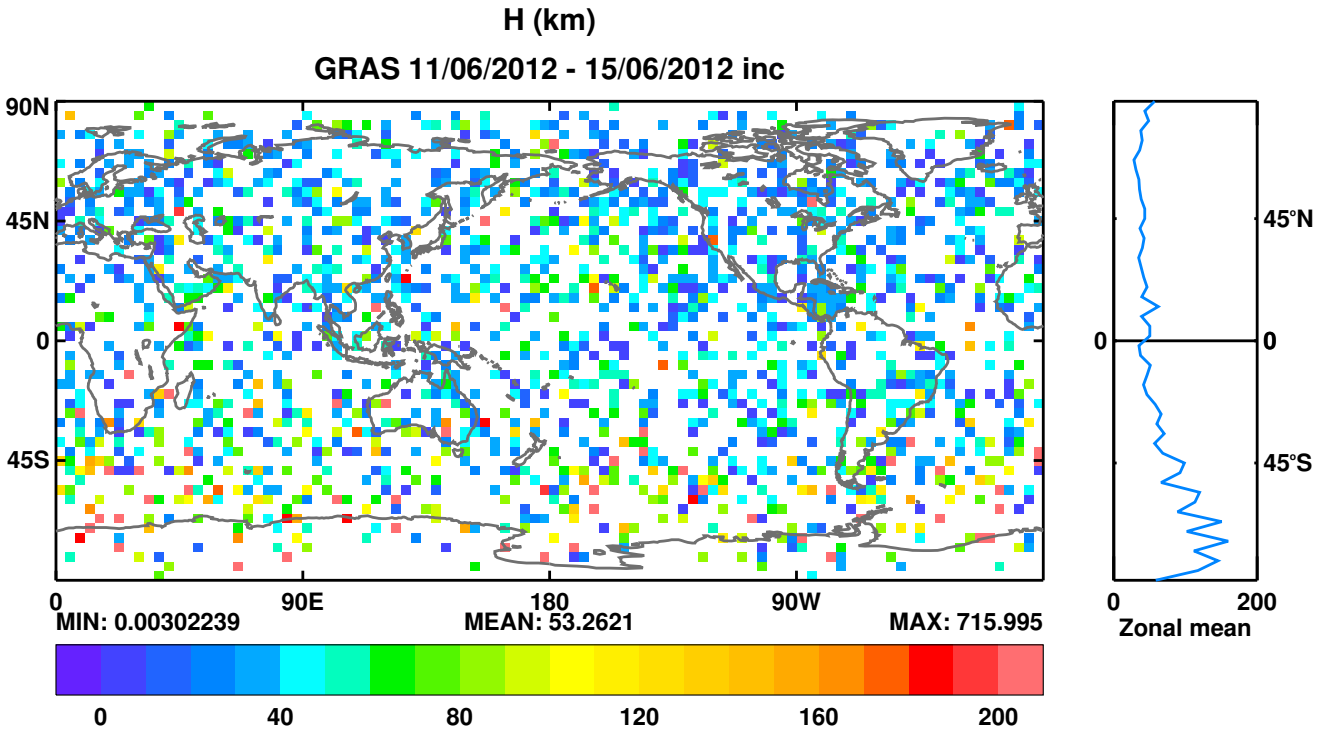

Figure 6.6: Global maps of retrieved Chapman layer width H from 2000 'good' least squares fits to the GRAS L1 – L2 bending angles between 11th and 15th June 2012.

7 Summary, conclusions and future work

This report has discussed several issues in connection with the modelling of the single frequency L1 and L2 bending angles by means of a simple model ionosphere. This has been motivated by the need to account for the not infrequent absence of one of the signals (usually L2, especially in the lower part of the profile). The current operational method, which consists of removing the ionospheric contribution to the bending by taking a linear combination of the L1 and L2 signals, cannot be applied in such situations. Using L1 and L2 separately would still be possible. The work of this report prepares the ground for a proper study of the value of doing so. Its key findings are as follows.

- ***Background theory, with and without a uniform horizontal refractivity gradient***
  - The basic theory for the frequency-dependent bending angles incurred by a radio wave when passing through a spherically symmetric ionosphere has been reviewed. The overall bending is proportional to the total electron content, TEC: the vertically integrated electron density $\int n_e(r)\,\mathrm{d}r$.
  - It has been pointed out that, for impact parameters beneath the ionosphere, the ray is always bent towards the Earth.
  - The impact of a uniform horizontal refractivity gradient has been examined by evaluating the first order perturbation to the spherically symmetric bending angles. It has been shown that large horizontal gradients can reverse the symmetrical ionosphere result and generate negative bending angles — that is, the ray can be deflected away from the Earth. According to this model, however, sufficiently large electron density gradients are unlikely to occur often enough to explain the observed abundance of these 'anomalous' bending angles.
  - The sensititivity of the bending angles to the assumed ionospheric electron density profile has been briefly examined. Below about 100 km there is little dependence on the shape of the electron density profile, save for an overall proportionality to the TEC. But if the lower side of the ionosphere encroaches on the upper end of the range of impact heights being studied it can strongly affect the bending angles. Generally, however, the single frequency bending angles 'flatten off' above about 50 km. This should be contrasted with the behaviour of the 'ionospherically corrected' bending angles, which are determined by the refractivity of the neutral atmosphere, and which continue to decay roughly exponentially with height beyond even 100 km.
- ***The bending produced by a Chapman layer ionosphere***
  - It has been shown that the bending angle induced by a model ionosphere which comprises a single, spherically symmetric ionosphere having a 'Chapman layer' electron density profile, Eqn (3.9), can be written (Eqn (4.2)) in terms of a function Z which depends only on the normalised relative distance between the impact height and the electron density peak.
  - Various methods of calculating Z have been examined (App A). The asymptotic behaviour of Z far above and far below the electron density peak have been described. A simple Padé approximation, which is correct to within 2.2% for all impact heights, has been derived.

- ***Applications to NWP***

  – Some idealised 1D–Var retrievals in a simple system comprising a dry, isothermal atmosphere with a Chapman layer ionosphere have been carried out. This model system has the virtue over real data that the 'true' state vector is known, which allows the reduction in its variance resulting from the retrieval procedure to be quantified.

  – The current operational procedure of using an ionospherically corrected linear combination of the two signals, LC, is compared to using both L1 and L2, using L1 alone, and to using L1 as a proxy for LC. Preliminary results tentatively suggest that making retrievals with the 'raw' signals L1 and L2 could deliver analysed temperatures and surface pressures that are clustered more tightly about the true values than those coming from the current ionospherically corrected signal. This appears to be true even if L1 alone is used. Either is much better than using L1 as a proxy for LC, which is currently the only option if one of the signals were permanently disabled.

  – 3500 consecutive L1 and L2 signals from the GRAS instrument on Metop-A had their differences, which are proportional to the ionospheric component of the bending, fitted to the Chapman layer Z function. The majority of the L2–L1 bending angle differences could be fitted satisfactorily, and the resulting ionospheric parameters (TEC, peak height and thickness) appear plausible. This is *not* to suggest that RO bending angles could be used to observe the ionosphere. Rather, it simply states that the 'effective' Chapman layer — the one that *could* generate the observed bending angles — is not wildly wrong.

  – A significant minority ($\sim$ 45%), however, of the L2–L1 bending angle differences could not be easily fitted to the Z function. Some of these ($\approx$ 13%) were because L2–L1 was in fact *negative* at height ($\geq$ 50 km). This is not possible within the framework presented here. Investigations continue into the cause of these 'anomalous' occultations. Horizontal electron density (and therefore refractivity) gradients is one possibility, but the earlier work of this report casts some doubt upon this. The concern is that the usual ionospheric correction, which renders these occulations nominally valid, is in fact masking a problem which should lead to the profile being excluded from the assimilation system. The matter needs to be resolved before undertaking serious assimilation trials.

- ***Future work***

  The work of this report could be extended in the following ways.

  – It should be possible to account for the effect of the refractive index not being unity at the LEO satellite, when estimating the bending angles from the Doppler shift values. For a stationary transmitter and a receiver in a circular orbit, this can be shown to introduce a bias in the bending angles α_i of the form (eg Schreiner et al, 1999 [15][1]):

$$\Delta\alpha_i \approx \frac{a}{\sqrt{r_{\mathrm{LEO}}^2 - a^2}} \frac{k_4}{f_i^2} n_e(r_{\mathrm{LEO}}), \tag{7.1}$$

  where $n_e(r_{\mathrm{LEO}})$, the electron density at the LEO satellite, could be estimated as part of the retrieval. The bending angle forward model could be modified to include this term. This correction is more important in single frequency retrievals, because the f^{-2} bias in Eqn (7.1) would cancel out if the usual ionospheric correction were applied to the L1 and L2 bending angles.

[1] Schreiner et al's expression (their Eqn (A6)) is twice as large as Eqn (7.1) because it applies to 'calibrated' bending angles — those between the LEO and its mirror image on the other side of the tangent point — rather than the GNSS-LEO bending angles considered here.

- It should also be possible to improve the accuracy of the forward model by removing the ionospheric bending from above the LEO satellite. For a Chapman layer, Figs A.2 and A.5 suggest that a correction based on a few terms of the Eqns (A.12) and (A.26) respectively should be adequate. This correction is likely to be more important for any reprocessing of CHAMP measurements, rather than COSMIC or GRAS, because the orbit has a significantly lower altitude (around 420 km, compared to around 800 km).
- More extensive investigations on the possible direct use of the L1 and/or L2 bending angles should be undertaken with real RO data. These studies could include O-B diagnoses, assimilation trials and comparisons with bending angles derived from ray-tracing codes.
- The puzzling abundance of 'anomalous' occultations — those in which the L1 bending angle exceeds the L2 bending angle — needs to be understood. Again, detailed comparison with ray-tracing codes could help here.
- Although it has been stressed that the simple ionospheric model described here is *not* intended to diagnose ionospheric parameters (even 'effective' ones), the temptation to examine, for example, the retrieved TECs resulting from a month-long assimilation trial, would be difficult to resist.
- Finally, the impact of other analytical electron density profiles (eg Fonda et al 2005, [8]) on the forward model accuracy could be investigated.

Acknowledgements

Useful discussions with Axel von Engeln, Christian Marquardt and Chris Burrows are gratefully acknowledged. Particular thanks are due to Mary Forsythe and John Eyre for reviewing it.

A Appendix A: The bending angles induced by a Chapman layer ionosphere

Recall that we are trying to calculate the bending angle (Eqn (2.1))

$$\alpha(a) = -2a \int_a^\infty \frac{\mathrm{d}\log n/\mathrm{d}x}{\sqrt{x^2-a^2}}\mathrm{d}x \tag{A.1}$$

where (Eqn (2.3))

$$\log n \approx n-1 = -k_4 n_e/f^2 \tag{A.2}$$

and (Eqn (3.9))

$$n_e(r) = \frac{\mathrm{TEC}}{\sqrt{2\pi}eH}\exp\left(\frac{1}{2}(1-u-e^{-u})\right), \tag{A.3}$$

in which $u = (r-r_0)/H$.

A.1 General theory

At typical ionospheric electron densities n_e of around 10^{11} m^{-3} at RO frequencies $f \sim 10^9$ Hz, Eqn (A.2) implies $n-1 \sim 10^{-6}$. We therefore replace $x = nr$ by r in the integrand of Eqn (A.1) to obtain, after substituting Eqn (A.2),

$$\begin{aligned}
\alpha(a,f) &= -2a\int_a^\infty \frac{\mathrm{d}\log n/\mathrm{d}r}{\sqrt{r^2-a^2}}\mathrm{d}r && \text{(A.4)}\\
&= 2a\frac{k_4}{f^2}\int_a^\infty \frac{\mathrm{d}n_e/\mathrm{d}r}{\sqrt{r^2-a^2}}\mathrm{d}r && \text{(A.5)}\\
&\approx 2a\frac{k_4}{f^2}\frac{2r_0}{(r_0+a)^{3/2}}\int_a^\infty \frac{\mathrm{d}n_e/\mathrm{d}r}{\sqrt{r-a}}\mathrm{d}r && \text{(A.6)}
\end{aligned}$$

where we approximately factorise $\sqrt{r^2-a^2}$ as $\sqrt{r-a}(r_0+a)^{3/2}/2r_0$ in the last step to ensure that Eqns (A.5) and (A.6) give the same result for an infinitely thin model ionosphere, $n_e(r) = \mathrm{TEC}\,\delta(r-r_0)$, which is an appropriate limit for this problem. Ionospheric bending angles calculated this way differ from (exceed) those calculated according to the more usual factorisation $\sqrt{r^2-a^2} \approx \sqrt{2a(r-a)}$ (eg Kursinski et al, 2000 [10]) by no more than 1%. Neither factorisation is 'correct', and this freedom of choice therefore places an irreducible uncertainty on any estimate of Eqn (A.4) whose integrand is simplified in this way. It follows that it is futile to calculate Eqn (A.1) more accurately than to within a per cent or so.

Substituting Eqn (A.3) into Eqn (A.6) gives, eventually,

$$\alpha_i(a) = \alpha(a,f_i) = \frac{k_4}{f_i^2}n_e^{max}\sqrt{\frac{4er_0^2a^2}{H(r_0+a)^3}}Z\left(\frac{r_0-a}{H}\right) \tag{A.7}$$

where the dimensionless, order 1, function Z is defined by

$$Z(l) = \int_{-l}^\infty \frac{(e^{-3u/2}-e^{-u/2})\exp(-\frac{1}{2}e^{-u})}{\sqrt{u+l}}\mathrm{d}u. \tag{A.8}$$

The function Z describes most of the variation of bending angle with height, since the other factors in Eqn (A.7) only vary slowly over the range of impact parameters a of interest. Crucially, Z depends only on the parameter $l = (r_0 - a)/H$, the distance from the peak of the Chapman layer expressed in widths of the layer. For practical RO applications, $2 \lesssim l \lesssim 10$.

Eqn (A.8), evaluated numerically at high precision, is plotted in grey in Fig A.1. Beneath the peak of the Chapman layer, at $l = 0$, the bending is positive and increasing with impact height; well above the peak it is negative and decreases (in magnitude) with height.

A.2 Solution for $l = (r_0 - a)/H \ll 0$

By expanding the super-exponential in Eqn (A.8) as a series of exponentials we find

$$Z(l) = \sum_{r=0}^{\infty} \frac{(-1/2)^r}{r!} \int_{-l}^{\infty} \frac{e^{-(r+3/2)u} - e^{-(r+1/2)u}}{\sqrt{u+l}} \, \mathrm{d}u \tag{A.9}$$

$$= 2\sum_{r=0}^{\infty} \frac{(-1/2)^r}{r!} \int_{0}^{\infty} \left(e^{(r+3/2)l} e^{-(r+3/2)v^2} - e^{(r+1/2)l} e^{-(r+1/2)v^2} \right) \mathrm{d}v \text{ (where } v^2 = u + l) \tag{A.10}$$

$$= \sqrt{2\pi e^{l'}} \sum_{r=0}^{\infty} \frac{(-e^{l'})^r}{r!} \left\{ \frac{2e^{l'}}{\sqrt{r+3/2}} - \frac{1}{\sqrt{r+1/2}} \right\} \tag{A.11}$$

$$= -2\sqrt{2\pi e^{l'}} \sum_{r=0}^{\infty} \frac{(-e^{l'})^r}{r!} \sqrt{r+1/2} \tag{A.12}$$

after a little algebra, and defining $l' = l - \log 2$. (The penultimate step uses the standard integral $\int_0^\infty \exp(-x^2)\,\mathrm{d}x = \sqrt{\pi}/2$.) Eqn (A.12) is a convergent series for all l' and therefore gives the full theoretical solution. In practice, however, for large l', the need to store the rapidly increasing and alternating terms at sufficient precision to calculate the small net total sets a limit to its utility. For example, with double precision arithmetic, the largest value of $l = (r_0 - a)/H = l' + \log 2$ for which direct summation of Eqn (A.12) is possible is about 4.0. For larger values of l the series diverges badly. Euler acceleration of the series — the transformation $e^{l'} \mapsto e^{l'}/(1 + e^{l'})$ followed by re-expression of the coefficents in the series (eg Mathews and Walker, 1970 [11]) — only extends this region of validity of l to about 4.6 (and at considerable calculational cost)[1]. For a thin ionospheric D-layer ($H \sim$ 10 km, $r_0 - R_E \sim$ 100 km), l could be as large as 10, and we are therefore forced to seek another solution in the large l regime.

These convergence characteristics are shown in Fig A.2, which plots the fractional error in Eqn (A.12) as a function of l and the number of terms in the series. Clearly an excellent solution for negative l is obtained by keeping just a few terms. Equally clearly, a very poor approximation is made for $l > 3$, no matter how many terms are kept in the partial sum.

A.3 Solution for $l = (r_0 - a)/H \gg 0$

In view of the numerical difficulties in evaluating Eqn (A.12) beyond l = 4.0, it is worth studying the behaviour of $Z(l)$ for large l directly.

Substituting $s^2 = (1/2)\exp(-u)$ in the integrand of Eqn (A.8), and then expanding the radical, shows

[1] With single precision arithmetic, the 'direct' and 'Euler' maximum computable ls fall to 3.0 and 3.1 respectively.

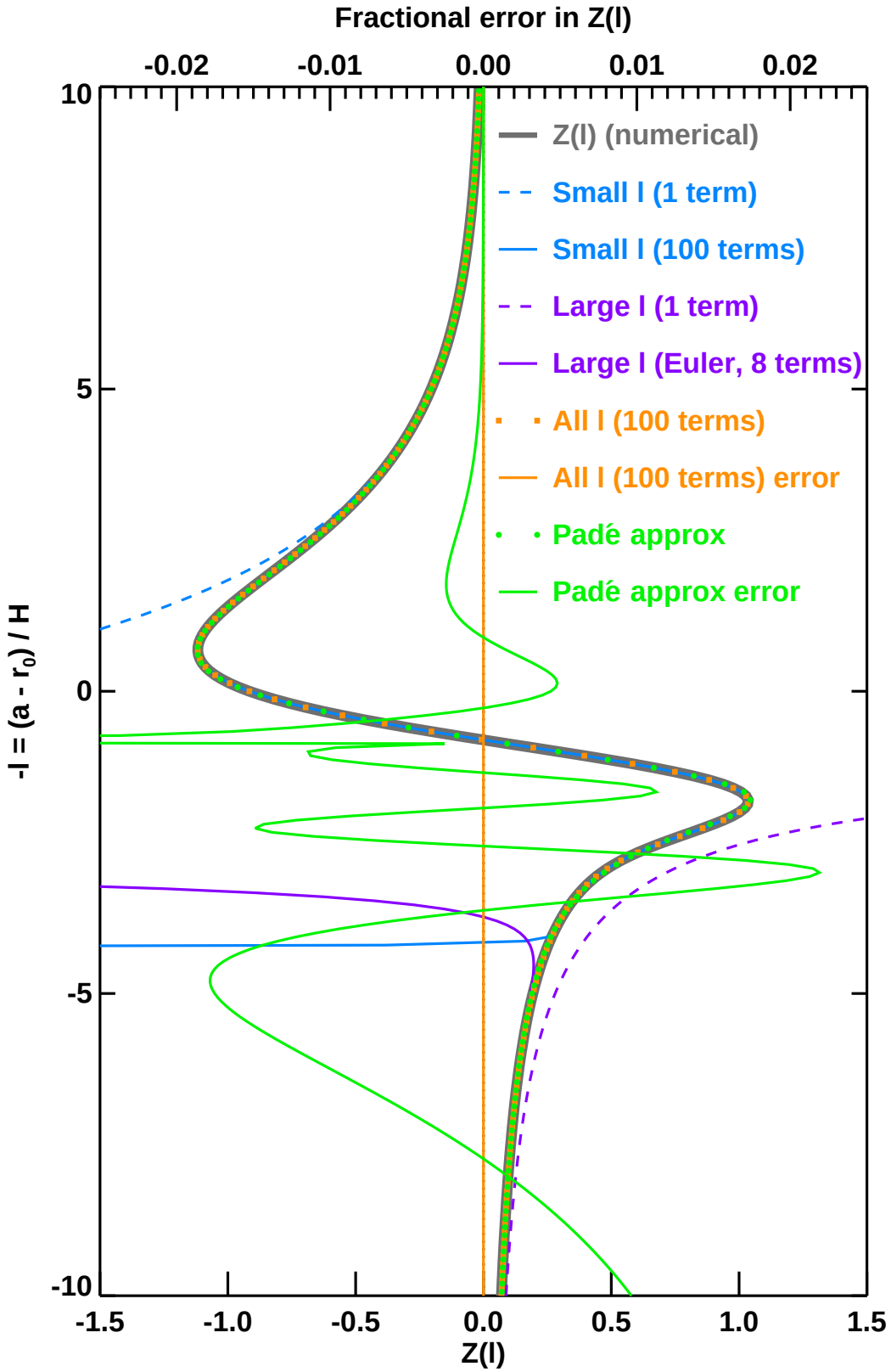

Figure A.1: Estimates of $Z(l)$: high precision numerical evaluation (Eqn (A.8)) — thick grey line; small l' approximation (Eqn (A.12)), 1 term — dashed blue line, 100 terms — solid blue line; large l' approximation (Eqn (A.18)), 1 term — dashed purple line, 8 terms of rearranged series (Eqn (A.22)) — solid purple line; all l' approximation (Eqn (A.26)), 100 term — orange square, 100 term error — orange line; Padé approximation (Eqn (A.27)), green disc, error — green line. Fractional error scale on top axis.

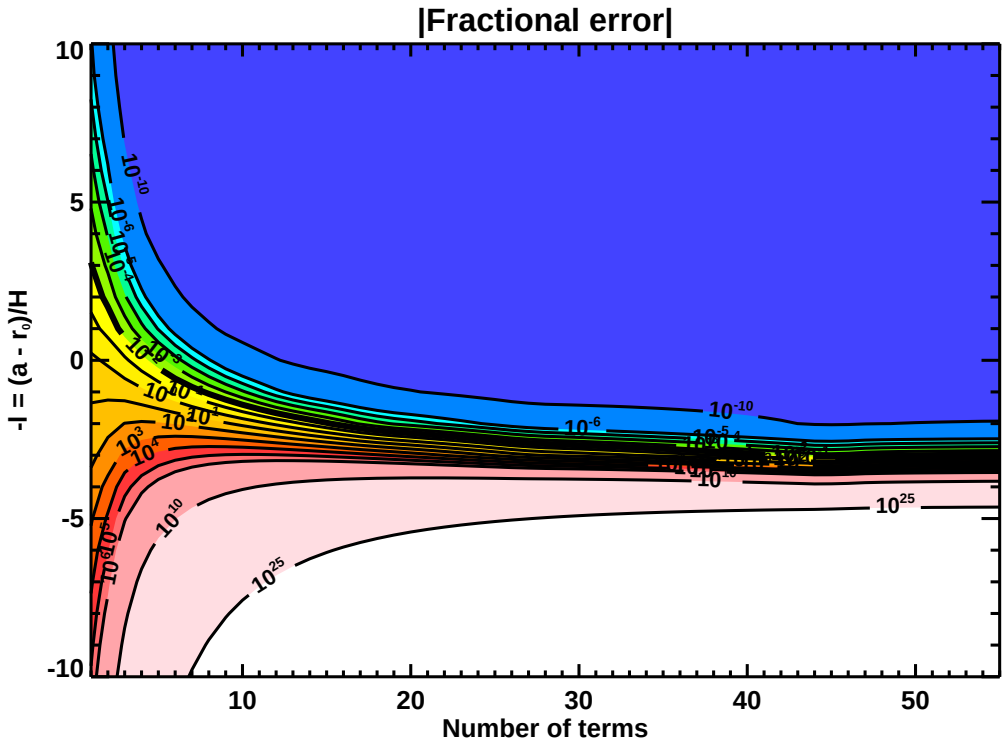

Figure A.2: Fractional error in Eqn (A.12) as a function of $l = (r_0 - a)/H$ and the number of terms in the partial sum. 1% contour in bold.

that

$$Z(l) = 2\sqrt{\frac{2}{l'}}\int_0^{\sqrt{g/2}} \frac{(2s^2-1)e^{-s^2}}{(1-2\log s/l')^{1/2}}\,\mathrm{d}s \tag{A.13}$$

$$= 2\sqrt{\frac{2}{\pi l'}}\sum_{r=0}^{\infty}\frac{\Gamma(r+1/2)}{\Gamma(r+1)}\left(2/l'\right)^r\int_0^{\sqrt{g/2}}\log^r s\,(2s^2-1)\,e^{-s^2}\,\mathrm{d}s \tag{A.14}$$

$$= 2\sqrt{\frac{2}{\pi l'}}\sum_{r=0}^{\infty}\frac{\Gamma(r+1/2)}{\Gamma(r+1)}\left(2/l'\right)^r\left\{\left[-se^{-s^2}\log^r s\right]_0^{\sqrt{g/2}} + r\int_0^{\sqrt{g/2}}\log^{r-1} s\;e^{-s^2}\,\mathrm{d}s\right\} \tag{A.15}$$

$$\sim 2\sqrt{\frac{2}{\pi l'}}\sum_{r=0}^{\infty}\frac{\Gamma(r+1/2)}{\Gamma(r+1)}\left(2/l'\right)^r r\int_0^{\infty}\log^{r-1} s\;e^{-s^2}\,\mathrm{d}s \quad \text{as } g\to\infty \tag{A.16}$$

$$= 2\sqrt{\frac{2}{\pi l'}}\sum_{r=1}^{\infty}\frac{\Gamma(r+1/2)}{\Gamma(r+1)}\left(2/l'\right)^r r\,2^{-r}\,\Gamma^{(r-1)}(1/2) \quad \text{(as the } r=0 \text{ term equals zero)} \tag{A.17}$$

$$= 2\sqrt{\frac{2}{\pi l'^3}}\sum_{r=0}^{\infty}\frac{\Gamma(r+3/2)}{\Gamma(r+1)}\Gamma^{(r)}(1/2)(l')^{-r} \quad \text{(letting } r\mapsto r+1\text{)} \tag{A.18}$$

$$= \sqrt{\frac{2\pi}{l'^3}}\left\{1-3(c+2\log 2)/2l' + 15\left((c+2\log 2)^2+\pi^2/2\right)/8l'^2+\ldots\right\} \tag{A.19}$$

$$\approx \sqrt{\frac{2\pi}{l'^3}}\left\{1.00-2.95/l'+16.48/l'^2-\ldots\right\} \tag{A.20}$$

Here, $\Gamma(x)=\int_0^\infty t^{x-1}e^{-t}\mathrm{d}t$ is the usual Gamma function, and $\Gamma^{(r)}(1/2)$ is its r^{th} derivative at $x=1/2$. $c\approx 0.57721\ 56649$ is the Euler-Mascheroni constant. See App B for details on the evaluation of these coefficients.

Eqn (A.18) shows that $Z \sim \sqrt{2\pi/l'^3} \sim \sqrt{2\pi/l^3}$ as $l' \to \infty$. Substitution into Eqn (A.7) shows that the bending angle in this limit is therefore

$$\alpha_i(a) = 2a\,\frac{k_4}{f_i^2}\,n_e^{max}\sqrt{2\pi e}H\,\frac{r_0}{(r_0^2-a^2)^{3/2}}. \tag{A.21}$$

This is of course the same as Eqn (3.2): the bending from a delta function ionosphere.

We note that Eqn (A.18) can also be obtained by formally integrating Eqn (A.8) by parts and discarding the 'integrated' part. The large l' assumption made in Eqn (A.16) is therefore equivalent to assuming $n_e(a)$ is so small that this procedure is legitimate. See the discussion around Eqn (2.5).

The first few $\Gamma^{(r)}(1/2)$, and their asymptotic form for large r, are tabulated in Table B.1 in App B. It follows from the latter (namely, $\Gamma^{(r)}(1/2) \sim (-1)^r 2^{r+1} r!$ as $r \to \infty$) that, not unusually, the asymptotic expansion Eqn (A.18) is divergent. This is clear from Fig A.3, which plots the fractional error in Eqn (A.18) as a function of $l = l' + \log 2$ and the number of terms of the series which are retained. For a given number of terms in the partial sum, the accuracy increases (eventually) as l' increases, but, for a given value of l', there is an optimum accuracy obtained by summing a certain number of terms. Including more terms in the partial sum worsens the accuracy. It is clear in this case that 1% accuracy is impossible for $l < 15$, and that even 10% accuracy is impossible for $l < 10$.

The one term solution, $Z(l) = \sqrt{2\pi/l'^3}$ — which, according to Fig A.3, is as good as it gets for $2 < l < 10$ — is included in Fig A.1. Clearly it is a poor approximation. In fact, one needs to be at least 15 scale heights below the Chapman layer peak before the delta function solution, $\propto l'^{-3/2}$, is within even 10% of the true value.

Convergence can be improved by applying the Euler transformation ([11]) to the series in Eqn (A.18). This gives

$$\begin{aligned}
Z(l) &= 2\sqrt{\frac{2}{\pi l'^3}}\sum_{r=0}^{\infty}\frac{\Gamma(r+3/2)}{\Gamma(r+1)}\Gamma^{(r)}(1/2)(l')^{-r} \\
&= 2\sqrt{\frac{2}{\pi l'^3}}\sum_{r=0}^{\infty}2^{-(r+1)}\sum_{s=0}^{r}\binom{r}{s}\frac{\Gamma(s+3/2)}{\Gamma(s+1)}\Gamma^{(s)}(1/2)(l')^{-s} \qquad \text{(A.22)} \\
&= \sqrt{\frac{2\pi}{l'^3}}\Big\{(1/2)+(1/4)\left[1-3(c+2\log 2)/2l'\right]+ \\
&\qquad (1/8)\left[1-3(c+2\log 2)/l'+15\left((c+2\log 2)^2+\pi^2/2\right)/8l'^2\right]+\ldots\Big\} \qquad \text{(A.23)} \\
&\approx \sqrt{\frac{2\pi}{l'^3}}\Big\{0.50+0.25(1-2.95/l')+0.125(1-5.90/l'+16.48/l'^2)+\ldots\Big\}. \qquad \text{(A.24)}
\end{aligned}$$

The convergence characteristics of Eqn (A.22), shown in Fig A.4, indicate that a 1% accurate solution for $l > 6$ is possible provided that at least 8 terms are included in the transformed series. It may therefore have some utility in the high l regime. Note, however, that the Euler acceleration has done nothing to prevent the ultimate divergence, and that the solution is still only valid for $l' > 0$. As we shall see in Sec A.4, there is a better solution which is valid for all l.

The 8 term partial sum in Eqn (A.22) is shown in Fig A.1. (The error is in fact negative.)

A.4 Theoretical solution for all $l = (r_0 - a)/H$

The numerical problems of Eqn (A.12) can be overcome by considering a *truncated* Chapman layer, in which $n_e(r)$ is given by Eqn (A.3) for $u > u_*$, and is zero below. We take $u_* = -3.5$ as this is large enough (the electron density is less than 10^{-6} of its peak value) to make a negligible difference (less

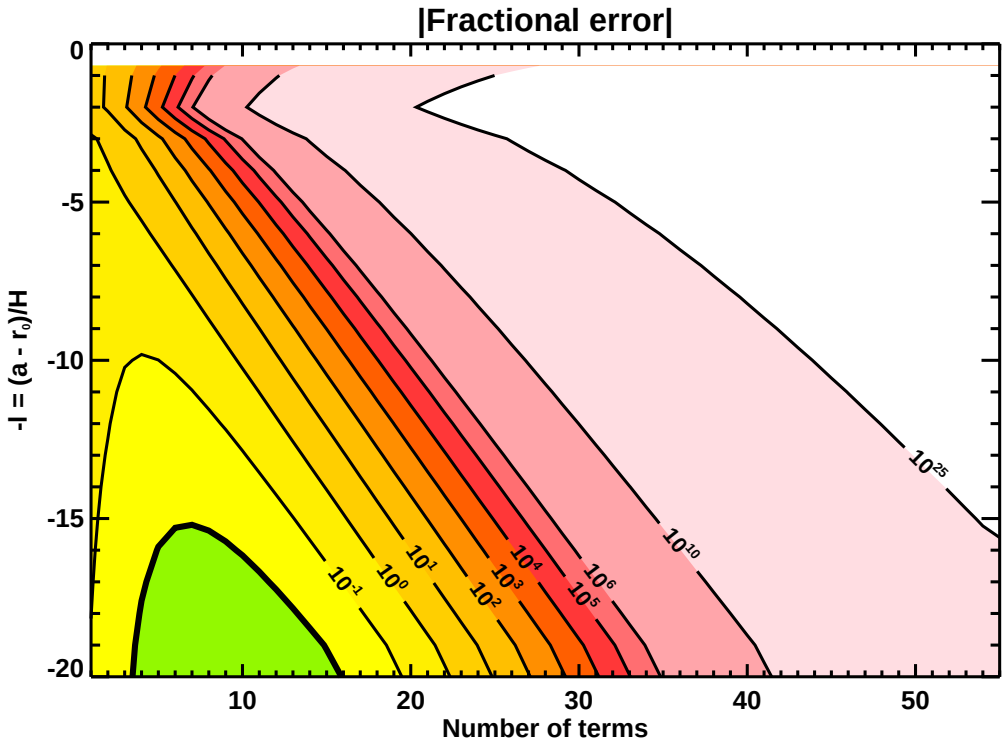

Figure A.3: Fractional error in Eqn (A.18) as a function of $l = (r_0 - a)/H$ and the number of terms in the partial sum. 1% contour in bold.

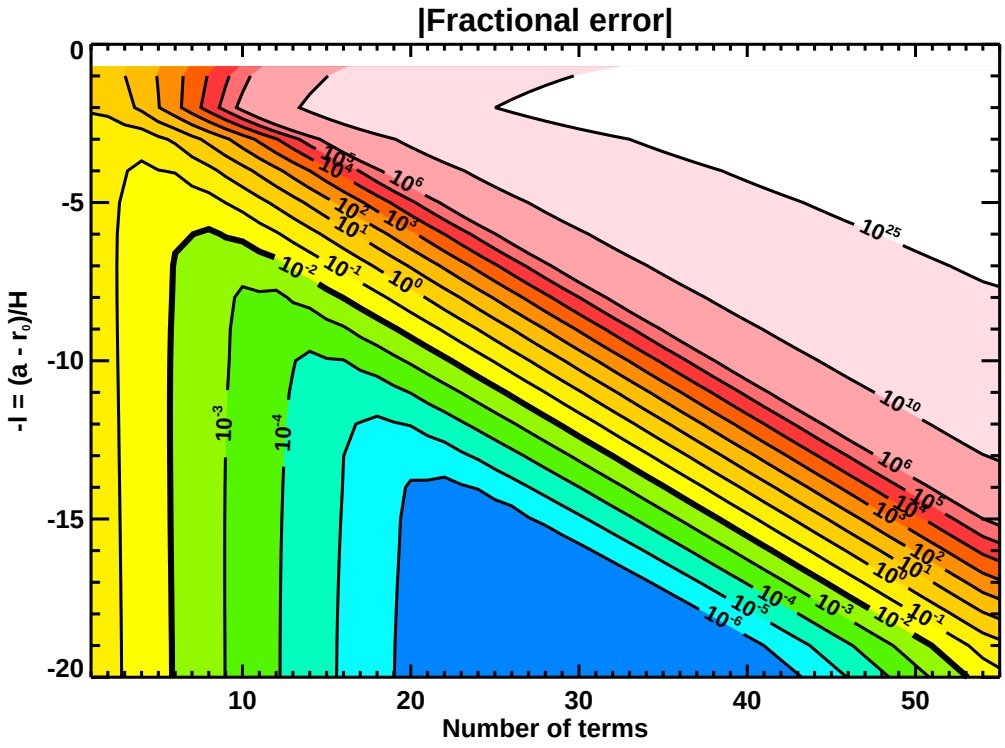

Figure A.4: Fractional error in Eqn (A.22) as a function of $l = (r_0 - a)/H$ and the number of terms in the partial sum. 1% contour in bold.

than 2 parts in 10^6)[2] to the large l' bending angles — the ones that are affected by the truncation — but small enough to prevent wildly oscillating terms appearing in Eqn (A.12), as we shall see. This value of u_* is also large enough to ensure that the TEC is largely unaffected by the truncation.

For a Chapman layer truncated at $u = u_*$ the theory of Section A.1 shows that

$$Z(l) = \int_{-l_*}^{\infty} \frac{(e^{-3u/2} - e^{-u/2})\exp(-\frac{1}{2}e^{-u})}{\sqrt{u+l}}\,\mathrm{d}u + 2S(l-l_*)\frac{\exp(-(u_*+e^{-u_*})/2)}{\sqrt{u_*+l}}, \tag{A.25}$$

where $l_* = \min(-u_*, l)$. Hence, if $l < -u_*$, $l = l_*$ and Eqn (A.25) matches Eqn (A.8). S is again the Heaviside step function: zero when its argument is less than or equal to zero, and unity otherwise. (It arises from differentiating the discontinuity in $n_e(r)$ at $u = u_*$ and integrating the resulting delta-function. We sidestep the singularity at $l = -u_*$ by insisting that $S(0) = 0$.)

Expanding the super-exponential as in Sec A.2, we find

$$\begin{aligned} Z(l) &= \sqrt{2\pi e^{l'_*}} \sum_{r=0}^{\infty} \frac{(-e^{l'_*})^r}{r!} \left\{ \frac{2e^{l'_*}}{\sqrt{r+3/2}}\,\mathrm{erfcx}\left(\sqrt{(r+3/2)(l-l_*)}\right) - \frac{1}{\sqrt{r+1/2}}\,\mathrm{erfcx}\left(\sqrt{(r+1/2)(l-l_*)}\right)\right\} \\ &+ 2S(l-l_*)\frac{\exp(-(u_*+e^{-u_*})/2)}{\sqrt{u_*+l}} \\ &= -2\sqrt{2\pi e^{l'_*}} \sum_{r=0}^{\infty} \frac{(-e^{l'_*})^r}{r!}\sqrt{r+1/2}\,\mathrm{erfcx}\left(\sqrt{(r+1/2)(l-l_*)}\right) + 2S(l-l_*)\frac{\exp(-(u_*+e^{-u_*})/2)}{\sqrt{u_*+l}} \end{aligned} \tag{A.26}$$

where $l'_* = l_* - \log 2 \le l - \log 2 = l'$ and the function $\mathrm{erfcx}\,(x) = \exp(x^2)\,\mathrm{erfc}\,(x)$ decreases *slowly* from 1 to 0 as x goes from 0 to infinity.

Some programming languages, such as IDL, provide $\mathrm{erfcx}\,(x)$ as an intrinsic function, which makes its evaluation quick and accurate. If such a verified intrinsic is not available, potential users of Eqn (A.26) should be aware that it needs a reasonably accurate evaluation of $\mathrm{erfcx}\,(x)$. For instance, the 50 term partial sum using the common approximation[3] $\mathrm{erfcx}\,(x) = 0.3480242t - 0.0958798t^2 + 0.7478556t^3$, where $t = (1 + 0.47047x)^{-1}$, loses the 1% accuracy shown in Fig A.5 beyond $l = 8$.

Notice that if $l \le -u_*$ — that is, above the truncation of the Chapman Layer — then $l'_* = l'$, the erfcx's equal unity, and Eqn (A.26) matches Eqn (A.12). But for $l > -u_*$, below the truncated Chapman Layer, Eqn (A.26) is an expansion in terms of the 'limited' parameter l'_*, which, since $-u_* < 4.0$, can be summed numerically (at double precision), as discussed in Sec A.2.

Because $u_* = -3.5$, the 'shoulder' term in Eqn (A.26), namely $2S(l-l_*)\exp(-(u_*+e^{-u_*})/2)/\sqrt{u_*+l}$, is negligible, and can be safely dropped in practice.

The convergence characteristics of Eqn (A.26) are shown in Fig A.5. It is clear that limiting l' to l'_* has curbed the wild behaviour of Eqn (A.12) for $l > 3$, and that a 1% accurate solution is possible even for $l = 10$ by retaining 50 terms in the partial sum. In fact, 60 terms give a solution accurate to within 1 part in 10^6.

The 100 term solution is included in Fig A.1, and clearly gives an accurate, if computationally expensive, solution to the problem.

[2] Because (cf Eqn (A.13)) $\int_{s_*}^{\sqrt{g/2}} (2s^2-1)e^{-s^2}(1-2\log s/l')^{-1/2}\,\mathrm{d}s \,/\, \int_0^{\sqrt{g/2}} (2s^2-1)e^{-s^2}(1-2\log s/l')^{-1/2}\,\mathrm{d}s \approx \mathrm{erfc}\,(s_*) + (2l'/\pi)s_*\exp(-s_*^2)$, as can be seen by expanding the square root in the integrand and keeping only the terms in l'^0 and l'^{-1}. If $u_* = -3.5$ then $s_* = \sqrt{\exp(-u_*)/2} \approx 4.1$, which means that $\mathrm{erfc}\,(s_*) \sim 10^{-8}$ and $s_*\exp(-s_*^2) \sim 10^{-7}$, so that if $l' \le 10$, the bending angle coming from the 'tail' of the integral beyond $s = s_*$ (ie coming from $u < u_*$ in Eqn (A.8)) is less than about 2×10^{-6} of the total.

[3] As (effectively) used in ROPP (http://www.romsaf.org/software.php).

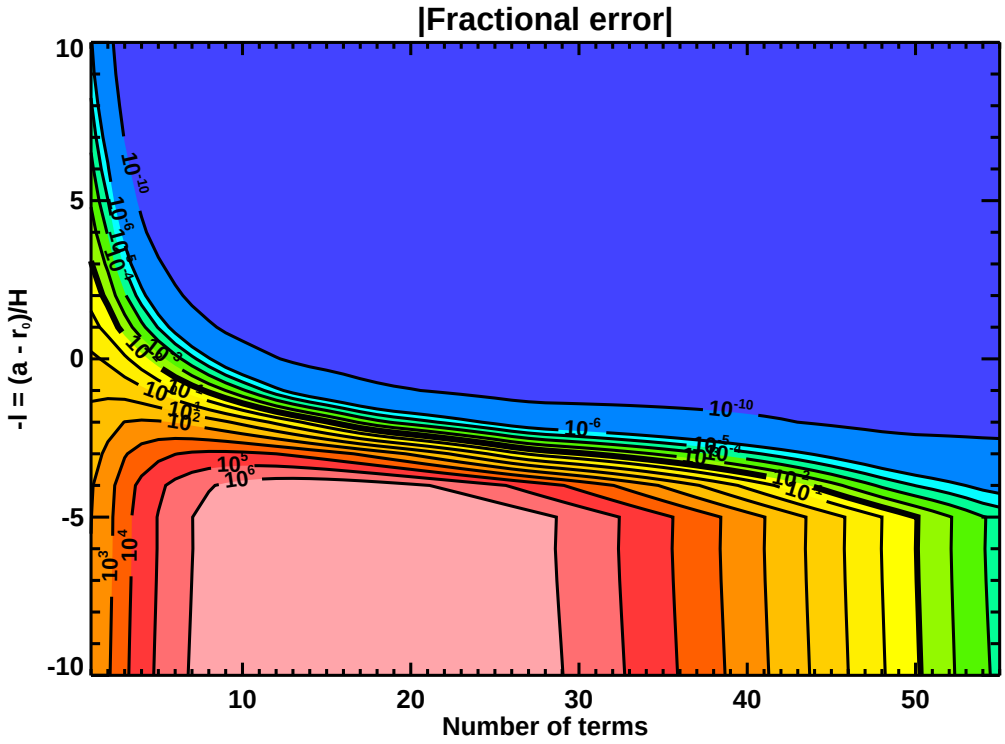

Figure A.5: Fractional error in Eqn (A.26) as a function of $l = (r_0 - a)/H$ and the number of terms in the partial sum. 1% contour in bold.

A.5 Practical solution for all $l = (r_0 - a)/H$

Eqn (A.26) may have some theoretical value and interest, but in practice a less accurate but quicker and simpler solution would suffice, bearing in mind the remarks in Sec A.1 about the irreducible uncertainty in the factorisation of $(r^2 - a^2)^{-1/2}$ in Eqn (A.5). The following Padé approximation in a transformed variable (θ) is much quicker to evaluate than direct numerical integration and is accurate to within 2.2% for all l[4]:

$$Z(l) \approx \tilde{Z}(\theta) = \sqrt{2\pi\theta}\,\frac{p_0 + p_1\theta + p_2\theta^2 + p_3\theta^3}{q_0 + q_1\theta + q_2\theta^2 + q_3\theta^3 + q_4\theta^4 + q_5\theta^5} \tag{A.27}$$

where $\theta(l') = \sinh^{-1}(e^{l'}) = \log\left(e^{l'} + \sqrt{1 + e^{2l'}}\right)$ and the coefficients $p_0 \ldots q_5$ are listed in Table A.1. The 'bridging function'[5] $\theta(l')$ is proportional to $e^{l'}$ for $l' \ll 1$ and to $l' + \log 2 = l$ as $l' \to \infty$, which, together with the conditions $p_0 = -\sqrt{2}$ and $p_3 = q_5$, encapsulate the correct asymptotic behaviours of $Z(l)$ as given by Eqns (A.12) and (A.18). This lends confidence to the integrity to the solution. The other coefficients are obtained by a least squares fit to the numerically integrated 'exact' solution. The real zeros of the denominator of Eqn (A.27) occur at negative values of θ and are therefore outside the domain of interest here. Eqn (A.27) is therefore well behaved numerically. It is also easy to differentiate, which is helpful when writing tangent linear and adjoint codes.

Eqn (A.27) and its fractional errors are plotted in Fig A.1. The largest error in the region not shown is 1.8% at $l \approx 20$.

[4] Except in the immediate vicinity of the zero of $Z(l)$ at $l \approx 0.8051$, where the fractional errors naturally get very large.
[5] Simpler bridging functions, like $\log(1 + l')$, did not deliver the same accuracy for the same number of tunable parameters.

Padé coefficients	
p_0	-1.41421360 ($=-\sqrt{2}$)
p_1	2.32540970
p_2	-1.11628850
p_3	0.23605387
q_0	1.00000000 ($=1$)
q_1	0.15210651
q_2	-0.76649105
q_3	1.26080520
q_4	-0.84687066
q_5	0.23605387 ($=p_3$)

Table A.1: Padé coefficients in Eqn (A.27)

A.6 Summary

The bending angle incurred by a ray passing through a spherically symmetric single Chapman layer model ionosphere has been calculated. Eqn (A.7) expresses it in terms of the function $Z(l)$, where $l=(r_0-a)/H$ is the distance of the impact parameter a from the Chapman layer peak height r_0, expressed in widths H of the Chapman layer.

Various solutions for $Z(l)$ have been found:

- Eqn (A.12), which is theoretically valid for all values of l, and very accurate for small l, but which suffers insurmountable numerical problems when l is greater than about 4.0;
- Eqn (A.18), which is asymptotically valid as $l\to\infty$ but of little use for the more modest values of l which occur in the RO context;
- Eqn (A.22), which is a rearrangement of Eqn (A.18) that can be more accurate for practical values of l, but which is still divergent and only asymptotically valid as $l\to\infty$;
- Eqn (A.26), which is an accurate (10^{-4}%) solution for a (very weakly) truncated Chapman layer, and which is calculable for all values of l;
- Eqn (A.27), which is a less accurate but simpler and quicker Padé approximation to $Z(l)$, which is accurate to within 2.2% for all l.

The following leading order asymptotic approximations have been derived:

$$Z(l)\sim\begin{cases}-\sqrt{2\pi e^l} & \text{as } l\to-\infty\\ \\ \sqrt{2\pi/l^3} & \text{as } l\to\infty.\end{cases} \tag{A.28}$$

$Z(l)$, and various approximations to it, are plotted in Fig A.1.

B Appendix B: Numerical coefficients in Chapman layer solution

B.1 Derivatives of the gamma function

The solution described in App A.3 requires the r^{th} derivative of the gamma function at argument 1/2, $\Gamma^{(r)}(1/2)$.

B.1.1 General r

The definition

$$\Gamma(a) = \int_0^\infty t^{a-1} e^{-t}\,\mathrm{d}t \quad \text{for } a > 0 \tag{B.1}$$

implies

$$\Gamma^{(r)}(1/2) = \int_0^\infty \log^r t\; t^{-1/2} e^{-t}\,\mathrm{d}t. \tag{B.2}$$

Calculation of $\Gamma^{(r)}(1/2)$ is effected by means of the digamma or ψ function, defined as

$$\begin{aligned} \psi(x) &= \Gamma'(x)/\Gamma(x) && \text{(B.3)}\\ &= -\left\{ c + x^{-1} + \sum_{r=1}^{\infty} \left[(r+x)^{-1} - r^{-1} \right] \right\}, && \text{(B.4)} \end{aligned}$$

where $c \approx 0.57721\ 56649$ is the Euler-Mascheroni constant (Sec 6.3, Abromowitz and Stegun, 1965 [1]).

Eqn (B.4) implies

$$\psi(1/2) = -(c + 2\log 2) \tag{B.5}$$

and

$$\psi^{(r)}(1/2) = (-1)^{r+1} r!\,(2^{r+1} - 1)\zeta(r+1) \quad \text{for } r > 0 \tag{B.6}$$

where $\zeta(r) = \sum_{s=1}^{\infty} s^{-r}$ is the Riemann zeta function.

Hence, by repeatedly applying $\Gamma'(x) = \Gamma(x)\psi(x)$, we find (all functions evaluated at argument 1/2):

$$\begin{aligned} \Gamma' &= \Gamma\psi && \text{(B.7)}\\ \Longrightarrow \Gamma'' &= \Gamma(\psi^2 + \psi') && \text{(B.8)}\\ \Longrightarrow \Gamma''' &= \Gamma(\psi^3 + 3\psi\psi' + \psi'') && \text{(B.9)}\\ \Longrightarrow \Gamma^{(4)} &= \Gamma(\psi^4 + 3\psi'^2 + 6\psi^2\psi' + 4\psi\psi'' + \psi''') && \text{(B.10)}\\ \Longrightarrow \Gamma^{(5)} &= \Gamma(\psi^5 + 10\psi^3\psi' + 15\psi\psi'^2 + 10\psi^2\psi'' + \\ &\quad 10\psi'\psi'' + 5\psi\psi''' + \psi'''') && \text{(B.11)}\\ \Longrightarrow \Gamma^{(6)} &= \Gamma(\psi^6 + 15\psi'(\psi'^2 + 3\psi'\psi^2 + \psi^4) + 10\psi''(\psi'' + 6\psi\psi' + 2\psi^3) + \\ &\quad 15\psi'''(\psi' + \psi^2) + 6\psi\psi'''' + \psi''''') && \text{(B.12)} \end{aligned}$$

and so on. c and the $\zeta(r)$ are tabulated (eg Table 23.3 Abromowitz and Stegun, 1965 [1]), which allow Eqns (B.5)–(B.12) to generate the values of $\Gamma^{(r)}(1/2)$ shown in Table B.1. Exact expressions for the first few values can also be obtained by appealing to the connection to the moments of the Chapman distribution, as discussed in Sec B.2. Later values (larger r) are easily calculated by direct numerical integration of Eqn (B.13) below.

B.1.2 Asymptotic limits as $r \to \infty$

Substituting $t = e^{-u}$ in Eqn (B.2) gives

$$\Gamma^{(r)}(1/2) = (-1)^r \int_{-\infty}^{\infty} u^r e^{-u/2} \exp(-e^{-u})\, \mathrm{d}u \tag{B.13}$$

$$= (-1)^r r^{r+1} \int_{-\infty}^{\infty} \exp\left[r(\log v - v/2)\right] \exp(-e^{-rv})\, \mathrm{d}v. \tag{B.14}$$

after writing $u = vr$.

As r increases, $\exp(-e^{-rv})$ becomes increasingly close to unity for $v > 0$ and increasingly close to zero for $v < 0$. We therefore approximate it by $S(v)$, the step function of v, in Eqn (B.14) to obtain

$$\Gamma^{(r)}(1/2) \approx (-1)^r r^{r+1} \int_{0}^{\infty} \exp\left[r(\log v - v/2)\right] \mathrm{d}v \quad \text{as } r \to \infty$$

$$= (-1)^r 2^{r+1} r!. \tag{B.15}$$

Further terms in the large r approximation to $\Gamma^{(r)}(1/2)$ can be found by expanding $\exp(-e^{-rv})$ in Eqn (B.14) and integrating term-by-term. The next one is $(-2/3)^{r+1} r!$.

The first few $\Gamma^{(r)}(1/2)$ are shown in Table B.1. Note the very rapid increase of $|\Gamma^{(r)}(1/2)|$ with r.

Chapman layer solution coefficients

r	$\Gamma^{(r)}(1/2)$	$\Gamma^{(r)}(1/2) - (-1)^r 2^{r+1} r!$
0	1.7724539	-0.22754615
1	-3.4802309	0.51976909
2	15.580177	-0.41982256
3	-94.768602	1.2313977
4	765.09180	-2.9082043
5	-7669.5235	10.476510
6	92118.681	-41.319287
$\to \infty$	$(-1)^r 2^{r+1} r!$	$(-2/3)^{r+1} r!$

Table B.1: Chapman layer solution coefficients.

B.2 Moments of the Chapman distribution

For the record, we note a connection between the derivatives of the Γ function at argument 1/2, and the moments of the Chapman distribution,

$$J_r = \int_{-\infty}^{\infty} u^r \exp[(1-u-e^{-u})/2]\,\mathrm{d}u. \tag{B.16}$$

By substituting $t = e^{-u}/2$ in Eqn (B.2), we find

$$\Gamma^{(r)}(1/2) = \frac{(-1)^r}{\sqrt{2e}} \sum_{s=0}^{r} \binom{r}{s} (\log 2)^{r-s} J_s \tag{B.17}$$

$$= \frac{(-1)^r}{\sqrt{2e}} (\log 2 + \uparrow)^r J_0, \tag{B.18}$$

where we define $\uparrow J_k$ to be J_{k+1} in the last rather formal expression.

Reciprocally,

$$J_r = (-1)^r \sqrt{2e} \sum_{s=0}^{r} \binom{r}{s} (\log 2)^{r-s} \Gamma^{(s)}(1/2) \tag{B.19}$$

$$= (-1)^r \sqrt{2e}\,(\log 2 + {}')^r\, \Gamma^{(0)}(1/2), \tag{B.20}$$

where we define ${}'\Gamma^{(k)}(1/2)$ to be $\Gamma^{(k+1)}(1/2)$ in the last equally formal expression.

This means that the J_r diverge for large r, as do the $\Gamma^{(r)}(1/2)$. In fact, it follows from Eqns (B.20) and (B.15) that

$$J_r \approx \sqrt{e}\, 2^{r+1}\, r! \quad \text{as } r \to \infty. \tag{B.21}$$

The first few J_r, and their asymptotic form for large r, are listed in Table B.2.

Moments of the Chapman distribution

r	J_r (theoretical)	J_r (numerical)	$J_r/\sqrt{e}2^{r+1}r!$
0	$\sqrt{2\pi e}$	4.1327314	1.2533141
1	$\sqrt{2\pi e}(c+\log 2)$	5.2500684	0.7960819
2	$\sqrt{2\pi e}\left((c+\log 2)^2+\pi^2/2\right)$	27.063704	1.0259354
3	$\sqrt{2\pi e}\left(14\zeta_3+3\pi^2(c+\log 2)/2+(c+\log 2)^3\right)$	155.74572	0.9840058
4	$\sqrt{2\pi e}\left(7\pi^4/4+56\zeta_3(c+\log 2)+3\pi^2(c+\log 2)^2+(c+\log 2)^4\right)$	1266.1382	0.9999371
$\to\infty$	$\sqrt{e}2^{r+1}r!$		1

Table B.2: Chapman layer moments, Eqn (B.16). $c \approx 0.57721\ 56649$ is the Euler-Mascheroni constant and $\zeta_3 \approx 1.20205\ 69032$ is the Riemann zeta function at argument 3. Also making a hidden appearance are $\zeta_2 = \pi^2/6$ and $\zeta_4 = \pi^4/90$.

C Appendix C: Reformulation of the calculation of $Z(l')$

We present a reformulation of the calculation of the $Z(l')$ function described in App A. This has the advantage that the whole problem can be reduced to the calculation of a definite integral whose asymptotic expansions for large and small l' can be calculated straightforwardly.

C.1 General theory

Recall that we are interested in calculating the function Z, defined in Eqn (A.13) as

$$Z(l') = 2\sqrt{\frac{2}{l'}}\int_0^{\sqrt{g/2}} \frac{(2s^2-1)e^{-s^2}}{(1-2\log s/l')^{1/2}}\,\mathrm{d}s, \tag{C.1}$$

where $l' = \log(g/2) = (r-r_0)/H - \log 2$.

Routine manipulations show that

$$\begin{aligned} Z &= 4\sqrt{2}\frac{\mathrm{d}}{\mathrm{d}l'}\int_0^{\sqrt{g/2}} (2s^2-1)e^{-s^2}(l'-2\log s)^{1/2}\,\mathrm{d}s & \text{(C.2)}\\ &= 4\sqrt{2}\frac{\mathrm{d}}{\mathrm{d}l'}\left\{\left[-se^{-s^2}(l'-2\log s)^{1/2}\right]_0^{\sqrt{g/2}} - \int_0^{\sqrt{g/2}} e^{-s^2}(l'-2\log s)^{-1/2}\,\mathrm{d}s\right\} \quad \text{(integrating by parts)}\\ &= -2\sqrt{2}x\frac{\mathrm{d}}{\mathrm{d}x}\left\{\sqrt{x}\int_0^1 e^{-xt}t^{-1/2}\log(1/t)^{-1/2}\,\mathrm{d}t\right\}, \quad \text{using } s^2 = xt \text{ where } x = g/2. & \text{(C.3)} \end{aligned}$$

Now, defining

$$\begin{aligned} J(x,c) &= \int_0^1 e^{-xt}t^{-1/2}\log(c/t)^{1/2}\,\mathrm{d}t & \text{(C.4)}\\ &= c^{1/2}\int_0^{1/c} e^{-xcs}s^{-1/2}\log(1/s)^{1/2}\,\mathrm{d}s \quad \text{(where } s = t/c\text{)}, & \text{(C.5)} \end{aligned}$$

$$\text{we find} \quad \left.\frac{\partial J(x,c)}{\partial c}\right|_{c=1} = (1/2)\int_0^1 e^{-xt}t^{-1/2}\log(1/t)^{-1/2}\,\mathrm{d}t \tag{C.6}$$

$$\text{and also} \quad \left.\frac{\partial J(x,c)}{\partial c}\right|_{c=1} = (1/2)\int_0^1 e^{-xt}t^{-1/2}\log(1/t)^{1/2}\,\mathrm{d}t - x\int_0^1 e^{-xt}t^{1/2}\log(1/t)^{1/2}\,\mathrm{d}t \tag{C.7}$$

by respectively differentiating Eqns (C.4) and (C.5) with respect to c and then setting $c = 1$.

Hence, by equating Eqns (C.6) and (C.7), we find

$$\int_0^1 e^{-xt}t^{-1/2}\log(1/t)^{-1/2}\,\mathrm{d}t = I + 2x\frac{\mathrm{d}I}{\mathrm{d}x} = 2\sqrt{x}\frac{\mathrm{d}}{\mathrm{d}x}\left(\sqrt{x}I\right) \tag{C.8}$$

where

$$I(x) = \int_0^1 e^{-xt}t^{-1/2}\log(1/t)^{1/2}\,\mathrm{d}t. \tag{C.9}$$

Putting Eqn (C.8) into Eqn (C.3) gives

$$Z = -4\sqrt{2}x\frac{\mathrm{d}}{\mathrm{d}x}\left\{x\frac{\mathrm{d}}{\mathrm{d}x}\left(\sqrt{x}I(x)\right)\right\} \tag{C.10}$$

$$= -4\sqrt{2x}\left\{x^2I''+2xI'+(1/4)I\right\} \quad \text{where } ' \text{ denotes } \mathrm{d}/\mathrm{d}x. \tag{C.11}$$

Eqn (C.11) shows that $Z(l')$ just depends on the monotonically decreasing function $I(x)$ defined by Eqn (C.9) and sketched in Fig C.2. The integrand of $I(x)$ is sketched in Fig C.1.

C.2 Small $x = g/2$

For $x \ll 1$ we can expand the exponent in Eqn (C.9) in powers of x to obtain

$$I(x) \sim \sum_{r=0}^{\infty}\frac{(-x)^r}{r!}\int_0^1 t^{r-1/2}\log(1/t)^{1/2}\,\mathrm{d}t \quad \text{as } x\to 0 \tag{C.12}$$

$$= \sum_{r=0}^{\infty}\frac{(-x)^r}{r!}\int_0^{\infty} 2s^2\exp(-(r+1/2)s^2)\,\mathrm{d}s \quad (\text{after substituting } s^2=\log(1/t)) \tag{C.13}$$

$$= \frac{\sqrt{\pi}}{2}\sum_{r=0}^{\infty}\frac{(-x)^r}{r!}(r+1/2)^{-3/2} \quad (\text{since } \int_0^{\infty}x^2e^{-x^2}\,\mathrm{d}x=\sqrt{\pi}/4) \tag{C.14}$$

$$= \sqrt{2\pi}\left\{1-\frac{x}{3\sqrt{3}}+\frac{x^2}{2!\,5\sqrt{5}}-\ldots\right\} \tag{C.15}$$

which implies, after substituting into Eqn (C.11),

$$Z \sim -2\sqrt{2\pi x}\left\{\sum_{r=2}^{\infty}\frac{(-x)^r}{r!}(r+1/2)^{-3/2}[r(r-1)+2r+1/4]+(1/4)(1/2)^{-3/2}-x(9/4)(3/2)^{-3/2}\right\} \text{ as } x\to 0$$

$$= -2\sqrt{2\pi x}\left\{\sum_{r=2}^{\infty}\frac{(-x)^r}{r!}(r+1/2)^{1/2}+\sqrt{1/2}-x\sqrt{3/2}\right\} \tag{C.16}$$

$$= -2\sqrt{2\pi x}\sum_{r=0}^{\infty}\frac{(-x)^r}{r!}(r+1/2)^{1/2} \tag{C.17}$$

$$= -2\sqrt{\pi x}\left\{1-\sqrt{3}x+\sqrt{5}x^2/2!-\ldots\right\}. \tag{C.18}$$

This is Eqn (A.12) again (recall that $x = g/2 = \exp(l')$). As before, it is in fact theoretically valid (convergent) for all $g/2$, although difficult in practice to sum numerically for the (large) values of $g/2$ that are needed in practice.

C.3 Large $x = g/2$

The extension to Watson's lemma (eq Sec 6.4, Bender and Orszag, 1999 [2]) given by Theorem 1.2, Chapter 9 of Olver, 1974 ([12]), namely

$$\int_0^1 e^{-xt}\left(\sum_{s=0}^{\infty}a_st^{(s+\lambda-\mu)/\mu}\right)\log^{\beta}(1/t)\,\mathrm{d}t \sim a_0\frac{\log^{\beta}x}{x^{\lambda/\mu}}\sum_{r=0}^{\infty}(-1)^r\binom{\beta}{r}\frac{\Gamma^{(r)}(\lambda/\mu)}{\log^r x} \quad \text{as } x\to\infty, \text{ for } \beta,\lambda,\mu>0, \tag{C.19}$$

shows that

$$I(x) \sim \sqrt{\frac{\log x}{x}}\sum_{r=0}^{\infty}(-1)^r\binom{1/2}{r}\frac{\Gamma^{(r)}(1/2)}{\log^r x} \quad \text{as } x\to\infty. \tag{C.20}$$

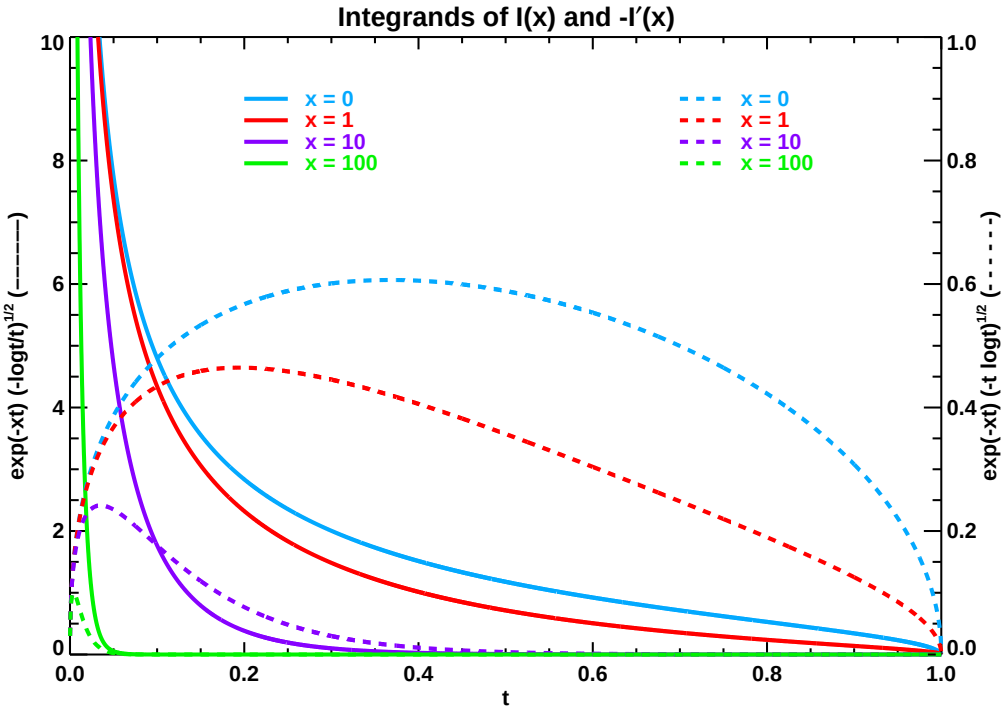

Figure C.1: Integrands of $I(0), I(1), I(10)$ and $I(100)$ (solid), as given by Eqn (C.9), and integrands of $-I'(0), -I'(1), -I'(10)$ and $-I'(100)$ (dashed), as given by Eqn (C.27).

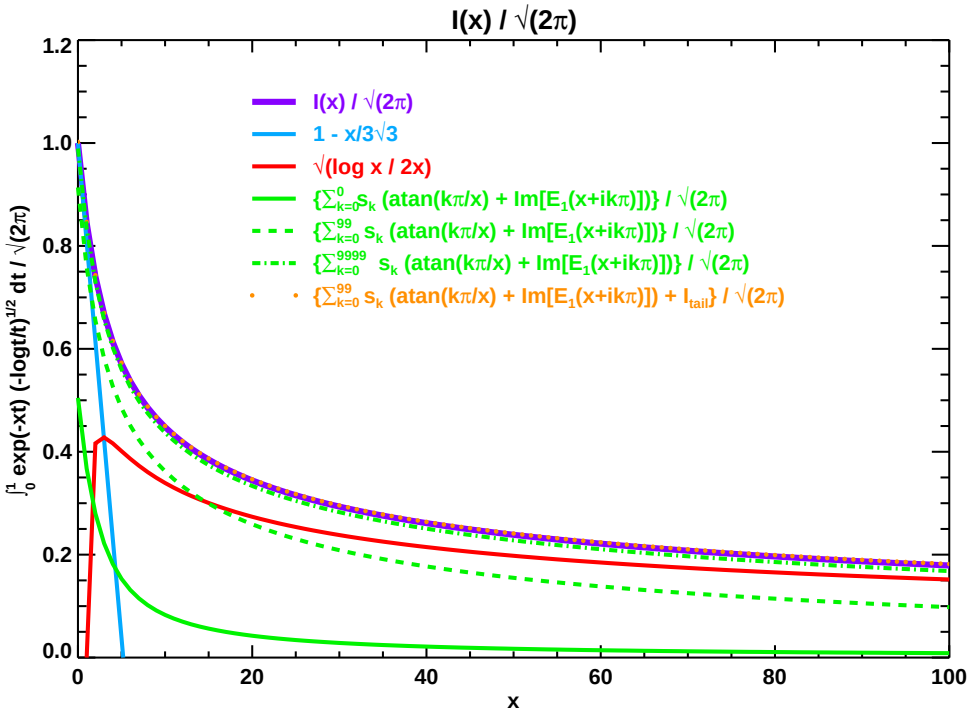

Figure C.2: $I(x)/\sqrt{2\pi}$, Eqn (C.9), and its leading order approximations for small x, Eqn (C.15), large x, Eqn (C.23), the 1, 100 and 10 000 term partial sums, for all x, Eqn (C.58) and the augmented 100 term partial sum, (C.63).

The ability to expand $I(x)$ in this way is the key reason for writing Z in terms of $I(x)$.

Since

$$\binom{1/2}{r} = \frac{(-1)^{r+1}(2r)!}{(2r-1)(2^r r!)^2}, \tag{C.21}$$

it follows that Eqn (C.20) can be rewritten as

$$I(x) \sim -\sqrt{\frac{\log x}{x}} \sum_{r=0}^{\infty} \frac{(2r)!}{(2r-1)(2^r r!)^2} \frac{\Gamma^{(r)}(1/2)}{\log^r x} \quad \text{as } x \to \infty \tag{C.22}$$

$$= \sqrt{\frac{\pi \log x}{x}} \left\{ 1 - \frac{\Gamma'(1/2)}{2\sqrt{\pi}\log x} - \frac{\Gamma''(1/2)}{8\sqrt{\pi}\log^2 x} - \ldots \right\} \tag{C.23}$$

where values of the r^{th} derivative of the gamma function at argument $1/2$, $\Gamma^{(r)}(1/2)$, are given in App B. (Substitution of Eqn (C.22) into Eqn (C.8), shows that Olver's theorem, Eqn (C.19), which is given for $\beta > 0$, in fact holds for $\beta = -1/2$ too. This is not surprising. The underlying theorem (Lemma 3 of Erdélyi, 1961 [6]) is true for all real β provided the upper limit of the integral is less than 1. If $\beta > -1$ the integral converges even if the upper range of integration is 1.)

Substituting Eqn (C.22) into Eqn (C.10) shows that (defining $y = \log x$)

$$Z \sim 4\sqrt{2}\frac{\mathrm{d}^2}{\mathrm{d}y^2} \left\{ \sum_{r=0}^{\infty} \frac{(2r)!}{(2r-1)(2^r r!)^2} \Gamma^{(r)}(1/2)\, y^{-r+1/2} \right\} \quad \text{as } x \to \infty \tag{C.24}$$

$$= \sqrt{\frac{2}{y^3}} \left\{ \sum_{r=0}^{\infty} \frac{(2r+1)!}{(2^r r!)^2} \Gamma^{(r)}(1/2)\, y^{-r} \right\} \tag{C.25}$$

$$= \sqrt{\frac{2\pi}{\log^3 x}} \left\{ 1 + \frac{3\Gamma'(1/2)}{2\sqrt{\pi}\log x} + \frac{15\Gamma''(1/2)}{8\sqrt{\pi}\log^2 x} + \ldots \right\}. \tag{C.26}$$

This is Eqn (A.18) again (note that $\Gamma(r+3/2)/\Gamma(r+1) = (\sqrt{\pi}/2)(2r+1)!/(2^r r!)^2$). As before, the first few terms are woefully inaccurate for the modest values of $l' = \log x$ needed in practice, and, because the series is divergent, adding more terms soon makes things even worse.

It is reassuring that the same expansion in inverse powers of l' appears by this method and by the method of Sec A.3. If there were a converging, or even a less rapidly diverging, expansion in (say) inverse powers of g, then Watson's lemma might be expected to have found it. Eqn (A.18) appears to be the best that can be done in the large l' limit of $Z(l')$.

C.4 General $g = x/2$

We note that formulating the problem in terms of $I(x)$ allows us to derive a theoretically exact solution to the original problem. Instead of $I(x)$ we examine

$$-I'(x) = \int_0^1 \exp(-xt)(-t\log t)^{1/2}\,\mathrm{d}t. \tag{C.27}$$

We now expand $(-t\log t)^{1/2}$, the dashed blue curve in Fig C.1, as a Fourier sine series:

$$(-t\log t)^{1/2} = \sum_{k=0}^{\infty} s_k \sin(k\pi t) \tag{C.28}$$

where

$$s_k = 2\int_0^1 (-t\log t)^{1/2} \sin(k\pi t)\,\mathrm{d}t. \tag{C.29}$$

The first 100 s_k, numerically calculated, are shown in Fig C.3. The oscillations result from the near symmetry of $(-t\log t)^{1/2}$ about $t=1/2$ (Fig C.1): if this function were exactly symmetric then the even coefficients s_{2m} would vanish. In fact, they are about half the size of their odd neighbours $s_{2m\pm1}$.

Also shown in Fig C.3 is the asymptotic form of s_k as $k\to\infty$, which can be estimated in the following way. The idea comes from a similar calculation of $\lim_{x\to\infty}\int_0^1 \log t\exp(ixt)\,\mathrm{d}t$ given in Example 1, Section 6.6 of Bender and Orszag, 1999 ([2]).

We consider

$$\int_{C_0}\exp(ik\pi t)(-t\log t)^{1/2}\,\mathrm{d}t \tag{C.30}$$

where C_0 is the contour in the complex t-plane from 0 to 1 along the line $\mathrm{Im}(t)=0$. We take the principal values of the logarithm and the square root. By Cauchy's theorem we can deform the integral along C_0 into the sum of integrals along three other contours: C_1, from $t=0$ to $t=i\infty$ along the line $\mathrm{Re}(t)=0$; C_2, from $t=i\infty$ to $t=1+i\infty$ along the line $\mathrm{Im}(t)=\infty$; and C_3, from $t=1+i\infty$ to $t=1$ along the line $\mathrm{Re}(t)=1$.

Along C_1 we write $t=is$, where s goes from 0 to ∞, and split the s integration range into three: $\int_0^{(k\pi)^{-2}}$, $\int_{(k\pi)^{-2}}^1$ and $\int_1^\infty$. For the first integral, we find

$$\begin{aligned}\int_0^{(k\pi)^{-2}}\ldots\,\mathrm{d}s &= i\int_0^{(k\pi)^{-2}} e^{-k\pi s}(-is\log(is))^{1/2}\,\mathrm{d}s &\text{(C.31)}\\ &= ie^{i\pi/4}\int_0^{(k\pi)^{-2}} e^{-k\pi s}\left(-s\log s\left(1+\frac{i\pi}{2\log s}\right)\right)^{1/2}\mathrm{d}s. &\text{(C.32)}\end{aligned}$$

Since we may assume $k\pi$ to be greater than $e^{\pi/4}$, $|\log s|>\pi/2$ over the range of integration, and we could therefore imagine expanding the radical in the integrand in inverse powers of the increasingly (as $k\pi\to\infty$) large quantity $\log s$. We also note that the minimum value of the exponential, $e^{-1/k\pi}$, is close to unity in the limit. To leading order, then,

$$\begin{aligned}\int_0^{(k\pi)^{-2}}\ldots\,\mathrm{d}s &\approx ie^{i\pi/4}\int_0^{(k\pi)^{-2}}(-s\log s)^{1/2}\,\mathrm{d}s &\text{(C.33)}\\ &= 2ie^{i\pi/4}\int_{\sqrt{2\log k\pi}}^\infty u^2\exp(-3u^2/2)\,\mathrm{d}u \quad \text{where } u^2=-\log s &\text{(C.34)}\\ &= ie^{i\pi/4}(1/9)\left(\sqrt{6\pi}\,\mathrm{erfc}\,\left(\sqrt{3\log k\pi}\right)+6\sqrt{2\log k\pi}/(k\pi)^3\right) &\text{(C.35)}\\ &= O(\sqrt{\log k\pi}(k\pi)^{-3}) \quad \text{as } k\pi\to\infty, &\text{(C.36)}\end{aligned}$$

because $\mathrm{erfc}\,(x)\sim e^{-x^2}/x\sqrt{\pi}$ as $x\to\infty$ (Eqn 7.1.23, Abromowitz and Stegun, 1965 [1]).

In the second integral we subsitute $u=k\pi s$ to obtain

$$\begin{aligned}\int_{(k\pi)^{-2}}^1\ldots\,\mathrm{d}s &= i(k\pi)^{-3/2}\int_{(k\pi)^{-1}}^{k\pi} e^{-u}u^{1/2}(-i\log(iu/k\pi))^{1/2}\,\mathrm{d}u &\text{(C.37)}\\ &= i(k\pi)^{-3/2}(i\log(k\pi/i))^{1/2}\int_{(k\pi)^{-1}}^{k\pi} e^{-u}u^{1/2}\left(1-\frac{\log u}{\log(k\pi/i)}\right)^{1/2}\mathrm{d}u. &\text{(C.38)}\end{aligned}$$

Over this range of integration, $|\log u/\log(k\pi)|<1$ which implies $|\log u/\log(k\pi/i)|<1$ since $|\log(k\pi/i)|>|\log(k\pi)|$. Hence we could expand the radical in inverse powers of the increasingly large number $\log k\pi$. The leading term as $k\pi\to\infty$ would be

$$\begin{aligned}\int_{(k\pi)^{-2}}^1\ldots\,\mathrm{d}s &\sim i(k\pi)^{-3/2}(i\log(k\pi/i))^{1/2}\int_{(k\pi)^{-1}}^{k\pi} e^{-u}u^{1/2}\,\mathrm{d}u &\text{(C.39)}\\ &= i(k\pi)^{-3/2}(i\log(k\pi/i))^{1/2}\left(\int_0^\infty u^{1/2}e^{-u}\,\mathrm{d}u+O((k\pi)^{-3/2})\right) &\text{(C.40)}\\ &= i(k\pi)^{-3/2}(i\log(k\pi/i))^{1/2}\left(\Gamma(3/2)=\sqrt{\pi}/2\right). &\text{(C.41)}\end{aligned}$$

The next term in Eqn (C.38) as $k\pi \to \infty$ would be

$$\int_{(k\pi)^{-2}}^{1} \dots \mathrm{d}s \sim i(k\pi)^{-3/2}\left(i\log(k\pi/i)\right)^{1/2}(-1/2\log(k\pi/i))\int_{(k\pi)^{-1}}^{k\pi} e^{-u}u^{1/2}\log u\,\mathrm{d}u \tag{C.42}$$

$$= i(k\pi)^{-3/2}\left(i\log(k\pi/i)\right)^{1/2}(-1/2\log(k\pi/i))\left(\int_0^\infty u^{1/2}e^{-u}\log u\,\mathrm{d}u + O(\log(k\pi)(k\pi)^{-3/2})\right)$$

$$= i(k\pi)^{-3/2}\left(i\log(k\pi/i)\right)^{1/2}(-1/2\log(k\pi/i))\Gamma'(3/2). \tag{C.43}$$

It follows from App B that $\Gamma'(3/2) = \Gamma(3/2)\psi(3/2)$ where $\psi(3/2) = \psi(1/2)+2 \approx 0.0365$. (This is small because $3/2 \approx 1.46163$, the positive zero of ψ (Sec 6.3.19, Abromowitz and Stegun, 1965 [1]).)

In the third integral we write $s = 1+u$ to obtain

$$\int_1^\infty \dots \mathrm{d}s = ie^{-k\pi}\int_0^\infty e^{-k\pi u}\left(-i(1+u)(i\pi/2+\log(1+u)\right)^{1/2}\mathrm{d}u \tag{C.44}$$

$$= ie^{-k\pi}\sqrt{\pi/2}\int_0^\infty e^{-k\pi u}\left((1+u)(1-(2i/\pi)\log(1+u)\right)^{1/2}\mathrm{d}u \tag{C.45}$$

$$= ie^{-k\pi}\sqrt{\pi/2}\int_0^\infty e^{-k\pi u}(1+O(u))\,\mathrm{d}u \tag{C.46}$$

$$\sim ie^{-k\pi}\sqrt{\pi/2}\,(k\pi)^{-1} \quad \text{as } k\pi \to \infty \text{ by Watson's lemma,} \tag{C.47}$$

and this is smaller than any inverse power of $k\pi$ in the limit.

Overall, then, from Eqns (C.36), (C.41), (C.43) and (C.47),

$$\int_{C_1}\exp(ik\pi t)(-t\log t)^{1/2}\,\mathrm{d}t \sim \frac{e^{3i\pi/4}}{(k\pi)^{3/2}}\left(\log(k\pi/i)\right)^{1/2}\sqrt{\pi}/2\,[1-\psi(3/2)/2\log(k\pi/i)] \text{ as } k\pi\to\infty. \tag{C.48}$$

The integral along C_2 vanishes as $t \to i\infty$ because of the $\exp(ik\pi t)$ factor.

Along C_3 we write $t = 1+is$ to get

$$\int_{C_3}\exp(ik\pi t)(-t\log t)^{1/2}\,\mathrm{d}t = i\int_\infty^0 e^{ik\pi}e^{-k\pi s}\left(-(1+is)\log(1+is)\right)^{1/2}\mathrm{d}s \tag{C.49}$$

$$\sim -ie^{-i\pi/4}(-1)^k\int_0^\infty s^{1/2}e^{-k\pi s}(1+O(s))\,\mathrm{d}s \quad \text{as } k\pi\to\infty \tag{C.50}$$

$$\sim -ie^{-i\pi/4}(-1)^k(k\pi)^{-3/2}\left(\Gamma(3/2)=\sqrt{\pi}/2\right), \tag{C.51}$$

by Watson's lemma.

Combining Eqns (C.48) and (C.51), we find from Eqn (C.29) that

$$s_k = 2\,\mathrm{Im}\int_{C_1+C_2+C_3}\exp(ik\pi t)(-t\log t)^{1/2}\,\mathrm{d}t \tag{C.52}$$

$$\sim \frac{\sqrt{\pi}}{(k\pi)^{3/2}}\,\mathrm{Im}\left\{e^{3i\pi/4}\left(\log(k\pi/i)\right)^{1/2}[1-\psi(3/2)/2\log(k\pi/i)] - ie^{-i\pi/4}(-1)^k\right\} \tag{C.53}$$

$$\approx (2\pi^2k^3)^{-1/2}\left\{\log(k\pi)^{1/2}+\log(k\pi)^{-1/2}[\pi/4-\psi(3/2)/2]-(-1)^k\right\}. \tag{C.54}$$

Eqn (C.54) is within 1% of the numerical value for $k > 65$. Note that it correctly captures the $(-1)^k$ oscillations of the true values. The 'DC' value of s_k as $k \to \infty$, that is, the one given by Eqn (C.54) but without the $(-1)^k$ contribution from contour C_3, is plotted in Fig C.3, as is a $k^{-3/2}$ curve for guidance. Since it follows from Eqn (C.54) that s_k is $O(\log(k\pi)^{1/2}k^{-3/2})$ as $k \to \infty$, comparison with the convergent series $\sum k^{-5/4}$ (for example) shows that $\sum s_k$ is convergent.

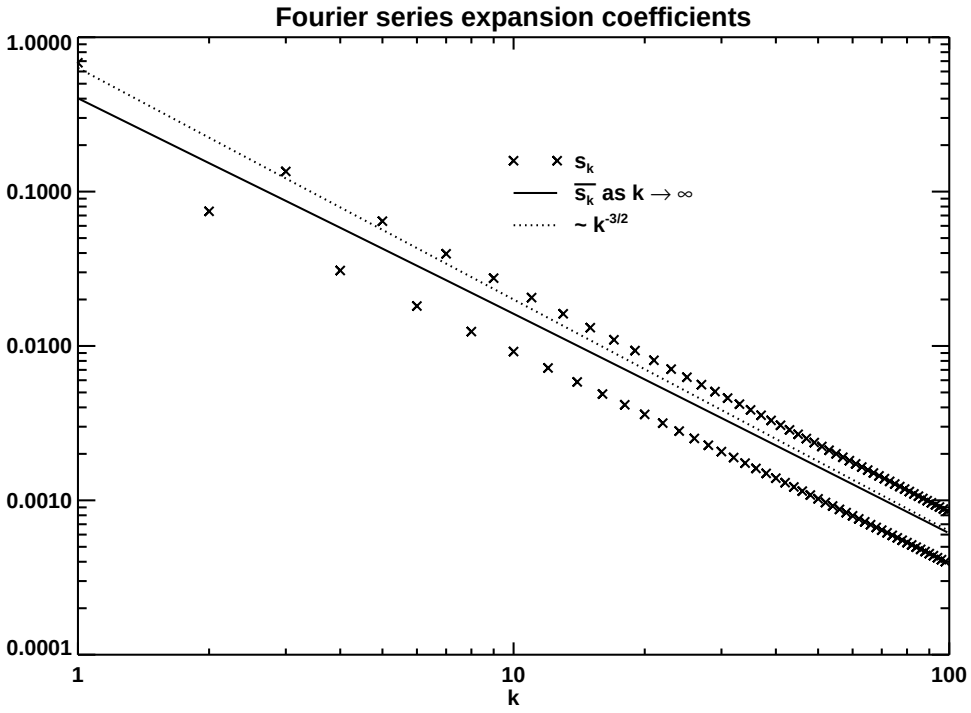

Figure C.3: Fourier series coefficients s_k defined by Eqn (C.29), and the asymptotic value as $k \to \infty$, given by Eqn (C.54) without the alternating $(-1)^k$ term.

Supposing then that the calculation/estimation of $\{s_k\}$ is settled, we can substitiute Eqn (C.28) into Eqn (C.27) to find

$$-I'(x) = \sum_{k=0}^{\infty} s_k \int_0^1 \exp(-xt)\sin(k\pi t)\,\mathrm{d}t \tag{C.55}$$

$$= \sum_{k=0}^{\infty} s_k \frac{k\pi}{(k\pi)^2+x^2}\left(1-(-1)^k e^{-x}\right) \tag{C.56}$$

which implies, since $I(\infty)=0$, that

$$I(x) = \sum_{k=0}^{\infty} s_k \int_x^{\infty} \frac{k\pi}{(k\pi)^2+y^2}\left(1-(-1)^k e^{-y}\right)\,\mathrm{d}y \tag{C.57}$$

$$= \sum_{k=0}^{\infty} s_k \left(\arctan\left(k\pi/x\right) + \mathrm{Im}\left(E_1(x+ik\pi)\right)\right) \tag{C.58}$$

since

$$\int_x^{\infty} \frac{\mathrm{d}y}{(k\pi)^2+y^2} = \frac{1}{k\pi}\left(\pi/2-\arctan\left(x/k\pi\right)\right) = \frac{1}{k\pi}\arctan\left(k\pi/x\right), \tag{C.59}$$

and (from Eqn 5.1.43, p 230, of Abromowitz and Stegun, 1965 [1])

$$\int_x^{\infty} \frac{e^{-y}}{(k\pi)^2+y^2}\,\mathrm{d}y = -\frac{1}{k\pi}\,\mathrm{Im}(e^{ik\pi}E_1(x+ik\pi)), \tag{C.60}$$

where

$$E_1(z) = \int_z^{\infty} \frac{e^{-t}}{t}\,\mathrm{d}t = -c-\log z - \sum_{l=1}^{\infty}\frac{(-z)^l}{l\,l!} \quad \text{for} \quad |\arg(z)|<\pi \tag{C.61}$$

is the (principal branch of the) exponential integral, and $c \approx 0.57721$ is the Euler-Mascheroni constant. Since $\arctan(k\pi/x) \sim \pi/2 - x/k\pi \to \pi/2$ and $E_1(x+ik\pi) \sim (-1)^k e^{-x}/k\pi \to 0$ as $k \to \infty$, and, as established above, $\sum s_k$ is a convergent series, it follows that Eqn (C.58) is a usable solution to the problem of calculating $I(x)$, and hence, from Eqn (C.11), $Z(l')$. It therefore gives an exact solution to the original problem.

In practice, however, Eqn (C.58) converges very slowly. This is clear from Fig C.2, which includes the 1, 100 and 10 000 term partial sums of Eqn (C.58)[1], which are respectively hopeless, 55% accurate and 94% accurate. (The last 9 000 Fourier coefficients for the final calculation were estimated using Eqn (C.54).)

This slow convergence can be explained and to some extent corrected by considering the large k behaviour of s_k (Eqn (C.54)) and of $\arctan(k\pi/x) + \mathrm{Im}(E_1(x+ik\pi))$. We find the leading order error in truncating Eqn (C.58) after $K \gg x/\pi$ terms to be

$$I_{\text{tail}}(x) \approx (2\pi^2)^{-1/2} \sum_{k=K}^{\infty} k^{-3/2} \left((\log k\pi)^{1/2} - (\log k\pi)^{-1/2} [\pi/4 - \psi(3/2)/2] \right) (\pi/2 - x/k\pi) \quad \text{(C.62)}$$

$$\approx \sqrt{\frac{\log K\pi}{2K}} \left\{ 1 + \frac{[1 + \pi/4 - \psi(3/2)/2]}{\log K\pi} + O((\log K\pi)^{-2}) \right\} - \frac{\sqrt{2}x}{3\pi^2} \sqrt{\frac{\log K\pi}{K^3}} \quad \text{(C.63)}$$

after approximating the sums by integrals and the resulting complementary error functions by the appropriate number of terms in their asymptotic expansions. The leading order behaviour, $\sqrt{\log(K\pi)/2K}$, suggests why even a 10 000 term partial sum fails to deliver 1% accuracy. The term proportional to x is formally of higher order in K^{-1}, but it can make a slight contribution to the sum if x is comparable to the truncation number K. For $K = 100$, Eqn (C.63) ranges from 0.2217 at $x = 0$ to 0.2102 at $x = 100$. When this is added to the 100 term partial sum it produces an estimate of $I(x)$ that is within 1.6% of the correct value for $0 \le x \le 100$ (see Fig C.2). This is much better than the unaugmented 10 000 term partial sum, which takes over 100 times longer to compute and is still 6% in error.

Eqns (C.58) and (C.63) therefore offer an interesting theoretical and tolerably accurate practical solution to the problem of calculating $I(x)$, at least for x between 0 and 100.

C.5 Summary

We have re-expressed the $Z(l')$ function of App A in terms of a simpler definite integral $I(g/2)$, defined in Eqn (C.9). It is intriguing that the problem can be reduced to such a simple form — and correspondingly frustrating that it does not appear to be expressible in simple closed form. Nonetheless, this integral does allow the approximate form of $Z(l')$ for small and large l' to be derived in a unified and fairly rigorous way. At the expense of some rather involved calculations, it also provides a formal solution for all l'.

[1] We evaluate $E_1(z)$ for complex z with the hybrid solution (see Chapter 5, Abromowitz and Stegun, 1965 [1])

$$E_1(z) = \begin{cases} -c - \log z - \sum_{l=1}^{10\lfloor |z| \rfloor} \frac{(-z)^l}{l l!} & \text{for } |z| \le 5 \\ \frac{e^{-z}}{z} \sum_{l=0}^{\lfloor |z| \rfloor - 1} \frac{l!}{(-z)^l} & \text{for } |z| > 5 \end{cases}$$

Bibliography

[1] Abromowitz M and Stegun I A, Handbook of Mathematical Functions: with Formulas, Graphs, and Mathematical Tables, Dover Publications, 1965.

[2] Bender C M and Orszag S A, Advanced Mathematical Methods for Scientists and Engineers: Asymptotic Methods and Perturbation Theory, Springer, 1999.

[3] Bureau of Meteorology, TEC global map, http://www.ips.gov.au/Satellite/2/2, 2014.

[4] Chapman S, The absorption and dissociative or ionizing effect of monochromatic radiation of an atmosphere on a rotating Earth, Proc Phys Soc, **43**, 483–501, 1931.

[5] The Coupled Thermosphere Ionosphere Plasmasphere Electrodynamics Model, Model TEC global map, http://helios.swpc.noaa.gov/ctipe/index.html, 2014.

[6] Erdélyi A, General asymptotic expansions of Laplace integrals, Arch. Rational Mech. Anal. **7**, 1, 1–20, 1961.

[7] Feynman R P, The Feynman Lectures on Physics, Volume II, Addison-Wesley, 1964.

[8] Fonda C, Coïsson P, Nava B and Radicella S M, Comparison of analytical functions used to describe topside electron density profiles with satellite data, Ann Geophys, **48**, 3, 491–495, 2005.

[9] Healy S B and Eyre J R, Retrieving temperature, water vapour and surface pressure information from refractive–index profiles derived by radio occultation: A simulation study, Quart Jour Roy Met Soc, **126**, 1661–1683, 2000.

[10] Kursinski E R, Hajj G A, Leroy S S and Herman B, The GPS Radio Occultation Technique, Terrestrial, Atmospheric and Oceanic Sciences, **11**, 1, pp53-114, 2000.

[11] Mathews J and Walker R L, Mathematical Methods of Physics, 2nd Edition, W A Benjamin, 1970.

[12] Olver F W J, Asymptotics and Special Functions, Academic Press, 1974.

[13] Rodgers C D, Inverse Methods for Atmospheric Sounding - Theory and Practice, World Scientific, 2000.

[14] The Radio Occultation Meteorology Satellite Application Facility, http://www.romsaf.org, 2014.

[15] Schreiner W S, Sokolovskiy S V, Rocken C and Hunt D C, Analysis and validation of GPS/MET radio occultation data in the ionosphere, Rad Sci, **34**, No 4, 949–966, 1999.

[16] Syndergaard S, private communication.

[17] von Engeln A, private communication.

[18] Zhang S R and Holt J M, Ionospheric Climatology and Variability from Long-term and Multiple Incoherent Scatter Radar Observations: Climatology in Eastern American Sector, J Geophys Res, **12**, A06328, doi:10.1029/2006JA012206, 2007.

ROM SAF (and earlier GRAS SAF) Reports

SAF/GRAS/METO/REP/GSR/001	Mono-dimensional thinning for GPS Radio Occulation
SAF/GRAS/METO/REP/GSR/002	Geodesy calculations in ROPP
SAF/GRAS/METO/REP/GSR/003	ROPP minimiser - minROPP
SAF/GRAS/METO/REP/GSR/004	Error function calculation in ROPP
SAF/GRAS/METO/REP/GSR/005	Refractivity calculations in ROPP
SAF/GRAS/METO/REP/GSR/006	Levenberg-Marquardt minimisation in ROPP
SAF/GRAS/METO/REP/GSR/007	Abel integral calculations in ROPP
SAF/GRAS/METO/REP/GSR/008	ROPP thinner algorithm
SAF/GRAS/METO/REP/GSR/009	Refractivity coefficients used in the assimilation of GPS radio occultation measurements
SAF/GRAS/METO/REP/GSR/010	Latitudinal Binning and Area-Weighted Averaging of Irregularly Distributed Radio Occultation Data
SAF/GRAS/METO/REP/GSR/011	ROPP 1dVar validation
SAF/GRAS/METO/REP/GSR/012	Assimilation of Global Positioning System Radio Occultation Data in the ECMWF ERA-Interim Re-analysis
SAF/GRAS/METO/REP/GSR/013	ROPP PP validation
SAF/ROM/METO/REP/RSR/014	A review of the geodesy calculations in ROPP
SAF/ROM/METO/REP/RSR/015	Improvements to the ROPP refractivity and bending angle operators
SAF/ROM/METO/REP/RSR/016	Simplifying EGM96 undulation calculations in ROPP
SAF/ROM/METO/REP/RSR/017	Simulation of L1 and L2 bending angles with a model ionosphere
SAF/ROM/METO/REP/RSR/018	Single Frequency Radio Occultation Retrievals: Impact on Numerical Weather Prediction
SAF/ROM/METO/REP/RSR/019	Implementation of the ROPP two-dimensional bending angle observation operator in an NWP system
SAF/ROM/METO/REP/RSR/020	Interpolation artefact in ECMWF monthly standard deviation plots
SAF/ROM/METO/REP/RSR/021	5th ROM SAF User Workshop on Applications of GPS radio occultation measurements
SAF/ROM/METO/REP/RSR/022	The use of the GPS radio occultation reflection flag for NWP applications

ROM SAF Reports are accessible via the ROM SAF website: http://www.romsaf.org